Received: Added at production | Revised: Added at production | Accepted: Added at production

DOI: xxx/xxxx

ARTICLE TYPE

A robust decomposed system control for an electro-mechanical linear actuator mechanism under input constraints

Mehdi Heydari Shahna | Mohammad Bahari* | Jouni Mattila

Faculty of Engineering and Natural Sciences, Tampere University, Tampere, Finland

Correspondence
*Mohammad Bahari.
Email: mohammad.bahari@tuni.fi

Present Address
Faculty of Engineering and Natural Sciences, Tampere University, 33100 Tampere, Finland

Funding Information
This work was supported by the Business Finland partnership project "Future all-electric rough terrain autonomous mobile manipulators" (Grant No. 2334/31/2022).

Abstract

This paper aims to develop a robust decomposed system control (RDSC) strategy under input constraints for an electro-mechanical linear actuator (EMLA) with model uncertainty and external disturbances. At first, a state-space model of a complex multi-stage gearbox EMLA system, driven by a permanent magnet synchronous motor (PMSM), is developed, and the non-ideal characteristics of the ball screw are presented through the model. This results in a six-order nonlinear strict-feedback form (NSFF) system that is decomposed into three subsystems. As the paper's main result, a novel RDSC strategy with uniform exponential stability for controlling subsystem states is presented. This developed controller avoids the "explosion of complexity" problem associated with backstepping by treating the time derivative of the virtual control input as an uncertain system term. The proposed method, while assuming load disturbances and input constraints with arbitrary bounds, offers a straightforward control approach for a broader range of applications. The controller's performance is evaluated through the simulation of two distinct duty cycles, each representing different levels of demand on the actuator facing load disturbances near the rated motor performance.

KEYWORD
electro-mechanical linear actuator; permanent magnet synchronous motor; robust control; adaptive control

1 | INTRODUCTION

The robotics industry is projected to dominate the upcoming decade, as well as to experience considerable market growth. As such, advanced robotic systems are receiving significant attention from both academia and industry, especially concerning their essential role in the development of autonomous technology and battery electric vehicles (BEVs) to enhance the efficiency, safety, and sustainability of mobility.[1,2,3] Mobile manipulators, which are robotic arms mounted on wheeled platforms for industrial use, can benefit from the development of BEVs, as these systems capable of performing a wide range of tasks in various environments, from manufacturing and logistics to search and rescue operations and beyond.[4] The on-board robotic arms of mobile manipulators can be equipped with hydraulic actuators, to enable their movement and manipulation capabilities. Hydraulic actuators are commonly used in mobile manipulators arms due to their high power-to-weight ratio. Although hydraulic actuators have been a mainstay in many industries for decades, utilizing them in mobile manipulators presents several challenges and limitations. The main drawback of hydraulic actuators is that they are energy-inefficient.[5] In addition, another disadvantage of hydraulic actuators is their susceptibility to leakage, which can lead to decreased pressure and performance.[6]

Electrified actuators have emerged as a popular alternative to hydraulic actuators due to their high potential performance. The

primary advantage of electrified over hydraulic actuators lies in their improved efficiency and fewer maintenance as well.[7] In addition, they offer more accurate control, as they integrate with sensors and advanced electronic control systems that enable greater precision when performing such tasks as lifting and moving heavy objects.[8,9] The ongoing trend towards electrification in the field of mobile manipulators has led to the emergence of electro-mechanical linear actuators (EMLAs) as an alternative to hydraulic actuators. EMLAs are a class of devices designed to transform electrical energy into linear motion, enabling the execution of various functions[10] and typically consisting of of several components, including a motor, lead screw or ball screw, nut, and load-bearing component.[11,12]

The motor is responsible for providing the required rotational force and the lead or ball screw is utilized to convert the rotational motion of the motor into linear motion. Permanent magnet synchronous motors (PMSMs) are a common motor type utilized in EMLAs due to their numerous benefits, including high power and torque density, allowing them to generate substantial force and power relative to their size.[13,14] In addition, PMSMs are highly efficient in converting electrical power into mechanical power, making them well-suited for energy-efficient applications, such as mobile manipulators, whose battery can store limited energy.[15,16]

EMLAs are considered a multidisciplinary problem, and their interaction creates intricate dynamics that are difficult to model for control design.[17]. Accurately modeling the multi-stage components of an EMLA is crucial because of their complex behavior, which can vary under different operating conditions such as variable loads and uncertainty in parameters. In particular, the ball screw exhibits nonlinear and non-ideal characteristics that must be considered in modeling and control design[17]. In this way, to simplify the structure of EMLAs, nonlinear strict-feedback form (NSFF) is a proper option, as it can mathematically express a cascade of functions, where each function takes its input the output from the previous function. The system input can be directly controlled, but the intermediate variables and system output are determined by the system dynamics. In general, NSFF systems are typically controlled using feedback control, such as adaptive control, nonlinear control, or backstepping control, among others. These methods enable easy modification of a part of the entire system and a separate investigation of the performance of each subsystem for high-quality results[18]. Hence, some recent research has utilized the NSFF control structure for the design of PMSM control to offer effective solutions to the challenges of achieving stability, tracking performance, and robustness in the presence of disturbances, uncertainties, and input constraints in PMSM control applications.[19,20,21]

In recent years, backstepping control, which is one method compatible with NSFF systems, has gained attention as a research area to address robust control in the electric machinery field, like PMSMs, due to its autonomy and ability to handle complex nonlinear systems, providing a straightforward way to design robust control systems. This recursive control method is based on the backstepping technique, which involves designing a sequence of controllers, each of which stabilizes one subsystem of the overall system.[22]. Furthermore, numerous studies in the literature have focused on enhancing the robustness of PMSMs using different types of adaptive backstepping control techniques. These methods have been demonstrated to possess significant potential for modeling complex systems and as adaptive controllers for nonlinear systems, as evidenced in previous works.[23,24,25] In the field of PMSM control, most research and studies have been conducted with a focus on velocity control. However, the current work is being discussed in a context focused primarily on position servocontrol.[26,27] Conversely, there is a drawback to backstepping algorithms, which can engender complexity, called "explosion of complexity" due to the repeated time derivative of the virtual control input, which should be solved in complex applications.[28] Hence, Lu and Wang[29] proposed the use of a fractional-order command filter for PMSMs to address this issue, and a the command filtering-based neural network control scheme was developed to handle input saturation in PMSMs. They, in another paper,[30] studied observer-based command-filtered adaptive neural network tracking control for a fractional-order chaotic PMSM subject to parameter uncertainties and external load disturbances. Likewise, to resolve the complexity of backstepping, they employed a command-filtering approach based on the first-order Levant differentiator. As we can see, most prior research tackled the issue by utilizing various filtering techniques. In contrast, the present work deviates from this approach and instead treats the time derivative of the virtual control input as an uncertain term in the system, without relying on any explicit filtering.

Precise measurements of electrical and mechanical parameters, including stator resistance and the friction coefficient, for PMSM, are often challenging. Moreover, commonly, the external load torque value is unknown and cannot be determined accurately. These factors highlight the critical need for the design of robust control methods, as the absence of robust control can jeopardize a system's performance and safety, as well as result in costly downtime or even catastrophic failure. Specifically, load disturbances can have a significant impact on the performance and stability of PMSMs, resulting in reduced efficiency, increased wear and tear, and potential damage to both the motor and the driven system. Hence, a nonlinear disturbance observer designed to estimate load disturbances by Liu, et al.[31] to regulate the PMSM speed when driving using backstepping control, combining the speed and current controllers. PMSM systems with unknown load torques were studied by Sun, et al.[19] and Ali, et al.[32]

proposing new adaptive backstepping control methods to address the position/speed tracking problem, while the method ensures asymptotic stability of the overall system. Although recent studies on PMSMs' control have emphasized addressing external disturbances and uncertainties, they have not adequately addressed the issue of input constraints, which is a common problem in PMSMs. Input constraints are crucial factors to consider in the control of PMSMs, owing to the inherent physical limitations on the input voltage and current of these motors. The application of control signals exceeding these limits can result in system instability, motor overheating, and permanent damage. Furthermore, the presence of load disturbances and model uncertainties can also cause the control signals to surpass the physical limitations of the motor. In such situations, it is imperative to design control systems that ensure stable and dependable operation of the motor while adhering to these constraints, thus enabling the operation of the motor within a safe and stable region and safeguarding it from damage. To address general disturbances and input saturation in PMSMs, Tan, et al.[33] proposed a sensorless robust optimal control scheme utilizing two neural network (NN)-based observers. The first observer was designed to estimate the back-electromotive force (EMF), while the second was designed to estimate the tracking errors of rotor position and speed in uniform boundedness.

As extensively discussed previously, in recent years, robust backstepping control has gained significant interest for PMSMs in NSFF structures. However, it has been observed that this control method has not been widely utilized in current studies concerning EMLAs actuated by PMSMs within NSFF structures. In addition, few studies have comprehensively addressed control problems pertaining to EMLAs, such as external disturbances, uncertainties, and input constraints. However, an adaptive backstepping tuning-function sliding-mode controller was proposed by Coban[34] for a class of NSFF systems to overcome quickly the varying parametric and unstructured uncertainties and avoid complexity. The effectiveness of the proposed controller was demonstrated by studying its implementation on an EMA system actuated by a DC motor. Although Lin and Lee[35] discussed linear induction motors (LIMs), these motors may not be directly relevant to our application. In addition, they have also not addressed input constraints in the EMA systems.

The present study makes several significant contributions to the field of EMLA control. Initially, this article introduced a modeling approach for a complex EMLA system with multi-stage gearbox, driven by a PMSM, that can generate all the required state variables for the design of control algorithms, including torques acting on the motor and force on the load side, to satisfy all conditions for achieving the prescribed dynamics. In addition, a robust control for the EMLA system is designed to achieve prescribed state responses by transforming the model into a six-order NSFF decomposed into three subsystems, while guaranteeing uniformly exponential bounded solutions, which has rarely been achieved. Furthermore, the proposed control approach is capable of avoiding the "explosion of complexity" problem without the need for filters, while remaining independent of the load conditions and accommodating input constraints. Finally, we present a comprehensive analysis of the EMLA in the NSFF system, which encompasses a variety of cycle duties utilizing the robust decomposed system control (RDSC) approach, such that the results of our analysis indicate that the control performance, including tracking accuracy and speed, is significant.

The remainder of the paper is organized as follows:

- Section 2 presents the various components of the EMLA servomechanism, along with the development of its analytical models to examine the energy conversions occurring within the system. The state-space model of the EMLA is then obtained by considering the aforementioned sub-models, and it is presented as a function of linear motion on the load side of the servomechanism to facilitate position control purposes. Finally, the specifications of the EMLA components, including the PMSM, gearbox, and screw, are listed at the end of this section.

- In Section 3, we investigate the control problems of the EMLA system, including input constraints, external disturbances, and uncertainties. To do so, we transform the EMLA system into a six-order NSFF system, consisting of three subsystems, the first of which is associated with the linear motion dynamic of the EMLA, while the second and third are associated with Park frame related to the PMSM.

- In Section 4, we define the RDSC and provide implementable equations to meet the requirements of the EMLA system. In addition, this section includes an extensive analysis of the uniformly exponential stability of all subsystems.

- The performance validity of RDSC is investigated in section 5 by considering two different types of cycle duties, depending on the type of load and the moment of loading and unloading, and the numerical performance of the RDSC for the EMLA is summarized in Table 3 and Table 4.

2 | ELECTRO-MECHANICAL LINEAR ACTUATOR MODELING

2.1 | Mathematical model of EMLA

This paper presents a study on an EMLA that utilizes a surface-mounted PMSM to convert the electric power to a mechanical one. The mathematical model for this EMLA is developed in the current section, and the system configuration is illustrated in Figure 1. The electric motor of the servomechanism is connected to a reduction gear, which in turn is coupled to a screw-nut mechanism to convert rotary motion into linear motion and to provide mechanical movement to the load. To simplify the process of modeling the EMLA, the paper considers three sub-models, namely the PMSM, the gears, and the screw–nut mechanisms, as follows:

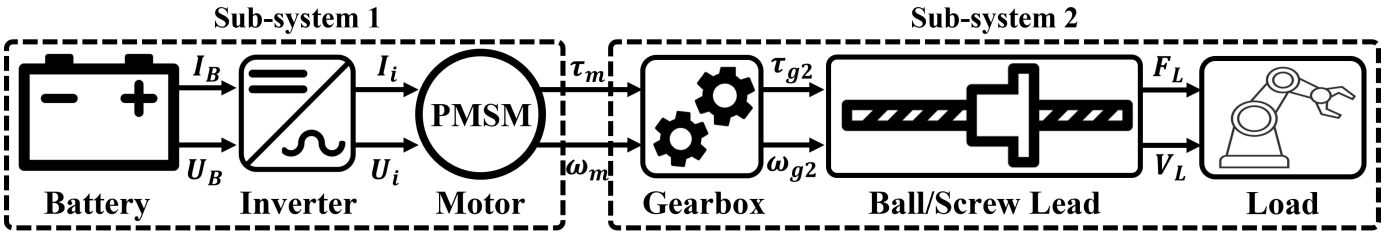

FIGURE 1 EMLA schematic.

2.1.1 | Permanent magnet synchronous motor

The rotary part of the PMSM is equipped with PMs, and their flux linking can be written in three ABC phases, as in (1):[36,37]

$$\begin{bmatrix} \psi_{aPM} \\ \psi_{bPM} \\ \psi_{cPM} \end{bmatrix} = \begin{bmatrix} \psi_{PM} cos(\theta_e) \\ \psi_{PM} cos(\theta_e - \frac{2\pi}{3}) \\ \psi_{PM} cos(\theta_e + \frac{2\pi}{3}) \end{bmatrix} \tag{1}$$

where ψ_{PM} is the PM flux linkage and θ_e is the electrical angle of the rotor. The total flux in each stator phase, which comprises the PM and three windings, can be calculated as a function of the self-inductance of the stator windings, the mutual inductance between stator windings, and the PM fluxes. This relationship is expressed in (2):

$$\begin{bmatrix} \psi_a \\ \psi_b \\ \psi_c \end{bmatrix} = \begin{bmatrix} L_{aa} & L_{ab} & L_{ac} \\ L_{ba} & L_{bb} & L_{bc} \\ L_{ca} & L_{cb} & L_{cc} \end{bmatrix} \begin{bmatrix} \psi_{aPM} \\ \psi_{bPM} \\ \psi_{cPM} \end{bmatrix} \tag{2}$$

Lastly, the voltage across the stator windings can be determined based on the magnetic flux change rate for each stator winding and the stator current, as given in (3):

$$\begin{bmatrix} V_a \\ V_b \\ V_c \end{bmatrix} = \begin{bmatrix} R_s & 0 & 0 \\ 0 & R_s & 0 \\ 0 & 0 & R_s \end{bmatrix} \begin{bmatrix} i_a \\ i_b \\ i_c \end{bmatrix} + \begin{bmatrix} \frac{d\psi_a}{dt} \\ \frac{d\psi_b}{dt} \\ \frac{d\psi_c}{dt} \end{bmatrix} \tag{3}$$

where the resistance of the stator winding is denoted as R_s. To eliminate the dependence of the PMSM's three-phase voltage on the rotor angle, the Park transformation (PT) can be utilized, as it converts the voltage from the ABC frame to the $dq0$ frame, as illustrated in equation (4).

$$\begin{aligned} u_d &= R_s i_d + L_d \frac{di_d}{dt} - P\omega L_q i_q \\ u_q &= R_s i_q + L_q \frac{di_q}{dt} + P\omega L_d i_d + P\omega \psi_{PM} \\ u_0 &= R_s i_0 + L_0 \frac{di_0}{dt} \end{aligned} \tag{4}$$

where L_d, L_q, and L_0 are inductance in the d-axis, q-axis, and zero sequence, respectively. In addition, ω is the mechanical rotational speed and P is the number of rotor PM pole pairs. Subsequently, the electromagnetic torque produced by the PMSM

can be expressed as (5):

$$\tau_m = \frac{3}{2} P i_q (\psi_{PM} + (L_d - L_q) i_d) \tag{5}$$

As the rotor of the studied surface-mounted PMSM has a non-salient shape, the inductances L_d and L_q are identical. Therefore, the torque equation can be simplified and expressed as a function of i_q, as obtained in (6).[38]

$$\tau_m = \frac{3}{2} P i_q \psi_{PM} \tag{6}$$

The linear momentum changes made to the moving parts of the EMLA in the motor side can be explained as (7):

$$\tau_m = J_m \ddot{\theta}_m + \tau_f + \tau_{g1} \tag{7}$$

where τ_m is the electromagnetic torque produced by the electric motor; J_m is the motor inertia; τ_f is the mechanical loss of the motor, including friction and windage; τ_{g1} is the input torque of the gearbox; and $\ddot{\theta}$ is the angular acceleration of the motor.

2.1.2 | Reduction gear

The relationship between the input and output torques of the gearbox is as follows (8):[39]

$$\tau_{g1} = \frac{n}{\eta_{GB}(\tau_{GB}, \omega_{GB})} \tau_{g2} \tag{8}$$

where n is gear ratio, τ_{g2} is the output torque of the gearbox, and η_{GB} is the efficiency of the gearbox. It is worth mentioning η_{GB} is a function of the applied torque and angular velocity of the gearbox. The gear ratio can be defined as (9):

$$n = \frac{n_1}{n_2} \tag{9}$$

where n_1 and n_2 are the numbers of input and output gear teeth. The output torque of the gears is coupled to the transmission system of the EMLA to deliver the power from the gears to the screw nut, and the motion equation can be considered as in (10):

$$\tau_{g2} = J_t \ddot{\theta}_t + b_t \dot{\theta}_t + \tau_{BS} \tag{10}$$

where J_t and b_t are the inertia and viscosity of the transmission system, respectively. In addition, $\ddot{\theta}_t$ and $\dot{\theta}_t$ are the angular acceleration and angular velocity of the transmission system, respectively, while τ_{BS} is the torque applied to the ball screw, and it will be calculated in section 2. A.3.

2.1.3 | Screw-nut mechanism

The screw-nut mechanism of an EMLA is responsible for converting the rotary motion into linear motion. The motion equation of a screw-nut can be written as (11):[40,41]

$$\tau_{BS} = \frac{\rho}{2\pi \eta_{BS}(\tau_{BS}, \omega_{BS})} F_{BS} \tag{11}$$

where the direct and reverse roller-screw efficiencies were obtained using (12):[42]

$$\begin{aligned} \eta_d &= \frac{1}{1 + (\frac{\mu}{tan\alpha})} \\ \eta_i &= 1 - \frac{\mu}{tan\alpha} \end{aligned} \tag{12}$$

where μ is the friction coefficient of the roller-screw and α is the lead angle of the roller-screw. For simplification, the coefficient of converting rotary movement to linear movement, called c_{RL}, is defined as in (13):

$$c_{RL} = \frac{2\pi}{n\rho} \tag{13}$$

where ρ is the ball screw pitch and η_{BS} is the efficiency of the ball screw. F_{BS} is the output force and can be computed as (14):

$$F_{BS} = m_{BS} \ddot{x}_L + b_{BS} \dot{x}_L + k_{BS} x_L + F_L \tag{14}$$

A mathematical model of the EMLA can be derived by developing motion equations between its different components. As a result, the electromagnetic torque of the electric motor can be written as in (15) as the function of linear motion at the end of EMLA ($\ddot{x}_L$,$\dot{x}_L$,x_L).

$$\tau_m = I_{eq} \ddot{x}_L + B_{eq} \dot{x}_L + K_{eq} x_L + f_{eq} F_L \tag{15}$$

where I_{eq}, B_{eq}, K_{eq}, and f_{eq} are the equivalent inertia, damping, spring effect, and load coefficient of the EMLA system. To form the two-mass model of the system, the inertia of the EMLA can be expressed at a single point, as in (16).

$$\frac{1}{2}I_{eq}\omega_m^2 = \frac{1}{2}J_m\omega_m^2 + \frac{1}{2}J_t\omega_t^2 + \frac{1}{2}M_{BS}\dot{x}_{BS}^2 \tag{16}$$

The speed of different components can be written with respect to the motor side, as in (17).

$$I_{eq} = J_m + n^2 J_t + \frac{M_{BS}}{c_{RL}^2} \tag{17}$$

Similarly, the equivalent stiffness at the motor side can be expressed as a function of motor twist as in (18).

$$\frac{1}{2}K_{eq}\Delta\theta_m^2 = \frac{1}{2}k_{\tau 1}\Delta\theta_m^2 + \frac{1}{2}k_{\tau 2}\Delta\theta_t^2 + \frac{1}{2}k_3\Delta x_{BS}^2 \tag{18}$$

By with considering $\Delta x = \frac{F}{k}$ and $\Delta\delta = \frac{\tau}{k_\tau}$, the stiffness of the system can be obtained using (19).

$$K_{eq} = \frac{1}{k_{\tau 1}} + \frac{1}{n^2 k_{\tau 2}} + \frac{c_{RL}^2}{k_3} \tag{19}$$

Finally, the equivalent viscosity of the entire system and the force coefficient can be written as in (20) and (21), respectively.

$$B_{eq} = [c_{RL}(b_m + \frac{n^2}{\eta_{GB}(\tau_{GB}, \omega_{GB})}b_t) + \frac{1}{c_{RL}}(\frac{1}{\eta_{BS}(\tau_{BS}, \omega_{BS})\eta_{GB}(\tau_{GB}, \omega_{GB}))}b_{BS}] \tag{20}$$

$$f_{eq} = \frac{1}{c_{RL}\eta_{GB}(\tau_{GB}, \omega_{GB})\eta_{BS}(\tau_{BS}, \omega_{BS})} \tag{21}$$

2.2 | State-space model of EMLA

To suit the control objectives, the state-space model equations are formulated in terms of the linear motion of the EMLA at the load side, and the equations for the derivatives of the motor current can be obtained using (22).

$$\begin{aligned}\frac{di_d}{dt} &= \frac{1}{L_d}(u_d - R_s i_d + Pc_{RL}\dot{x}_L 2L_q i_q)\\ \frac{di_q}{dt} &= \frac{1}{L_q}(u_q - R_s i_q - Pc_{RL}\dot{x}_L L_d i_d - Pc_{RL}\dot{x}_L\psi_{PM})\end{aligned} \tag{22}$$

The d-axis current, i_d, is controlled to track a reference value of zero in position control applications of PMSMs. In this study, the objective of the control is to maintain a constant load position while regulating i_d to follow the reference current $i_d^* = 0$. By setting i_d to zero, the magnetic field along the d-axis is eliminated, and the torque generated by the electric machine becomes independent of the rotor's position. As a result, the load position can be controlled without affecting the magnetic field along the d-axis. The q-axis current, i_q, can be used to generate the torque necessary for position control, and the time derivatives of the currents can be expressed in a simplified form, as shown in equation (23), which facilitates the design and analysis of the control system for the EMLA.

$$\begin{aligned}\frac{di_d}{dt} &= \frac{1}{L_d}(u_d + Pc_{RL}\dot{x}_L 2L_q i_q)\\ \frac{di_q}{dt} &= \frac{1}{L_q}(u_q - R_s i_q - Pc_{RL}\dot{x}_L\psi_{PM})\end{aligned} \tag{23}$$

In addition, the linear velocity and acceleration can be found using (24):

$$\begin{aligned}\dot{x}_L &= \frac{1}{c_{RL}}\dot{\theta}_m \\ \ddot{x}_L &= \frac{1}{I_{eq}}[\frac{3}{2}Pi_q\psi_{PM} - b_{eq}\dot{x}_L - k_{eq}x_L - f_{eq}F_L]\end{aligned} \tag{24}$$

The state vectors can be defined using (25) for the system:

$$X(t) = [i_d(t) \;\; i_q(t) \;\; \dot{x}_L \;\; x_L]^T \tag{25}$$

Input vectors (control variables) of the system are given in (26) :

$$U(t) = [u_d(t) \;\; u_q(t)]^T \tag{26}$$

Output vectors of the system can be defined using (27):

$$Y(t) = [i_d(t) \;\; i_q(t) \;\; \dot{x}_L \;\; x_L]^T \tag{27}$$

The load disturbance input of the system is considered the mechanical load of the EMLA, as in (28):

$$Z(t) = F_L \tag{28}$$

All the mentioned matrices form a continuous state-space model for EMLA powered by PMSM, which can be expressed as in (29), and A, B, and C can be obtained accordingly.

$$\begin{aligned}\dot{X}(t) &= AX(t) + BU(t) + CZ(t) \\ Y(t) &= DX(t) + EU(t) + FZ(t)\end{aligned} \tag{29}$$

In this paper, the PMSM adopted for the study case is the 400V 3.99kW Nidec PMSM servo motor. In addition, the ball screw BSG-ZUAZO model HLF "63x16-13-8-R". Characteristics of the EMLA components, including the motor, gearbox, and ball screw are listed in Table 1.

TABLE 1 PMSM and Gearbox Parameters

Parameter	Value	Unit
PMSM		
PM Magnetic Flux	0.357	Weber
Number of Pole Pairs	3	-
Rated Power	3.99	kW
Rated Current	7.9	A
Rated Torque	12.70	N.m
Motor Stall Torque	16.00	N.m
Motor Peak Torque	48.00	N.m
Rated Speed	3000	rpm
Phase Resistance	1.23	Ω
Phase Inductance	9.89	mH
Gearbox and BallScrew		
Gear Ratio	24.35	-
Gearbox Efficiency	96	%
Screw Lead	16	mm
Screw Diameter	63	mm
Screw Lead Angle	4.55	Degree°
Screw Efficiency	87	%

3 | PROBLEM FORMULATION AND PRELIMINARIES

In this section, the entire EMLA system, expressed in section 2, is transformed into a six-order NSFF, decomposed into three subsystems, each of which has two sub-subsystems, in consideration of control input constraints similar to[43] for subsystems, as follows:

$$\begin{aligned}
&\dot{x}_1 = x_2 + F_1(x_1) + d_1 \\
&\dot{x}_2 = g_2 S(i_q^*) + F_2(x_1, x_2) + d_2 \\
&\cdots\cdots\cdots\cdots\cdots\cdots\cdots\cdots \\
&\dot{x}_3 = x_4 + F_3(x_1, ..., x_3) + d_3 \\
&\dot{x}_4 = g_4 S(u_d) + F_4(x_1, ..., x_4) + d_4 \\
&\cdots\cdots\cdots\cdots\cdots\cdots\cdots\cdots \\
&\dot{x}_5 = x_6 + F_5(x_1, ..., x_5) + d_5 \\
&\dot{x}_6 = g_6 S(u_q) + F_6(x_1, ..., x_6) + d_6
\end{aligned} \tag{30}$$

For ($k = 1, ..., 6$), x_k are states of subsystems, F_k are uncertainties, and d_k are external disturbances, including load effects, where F_k and d_k are assumed nonlinear and unknown. According to Table 1, regarding the PMSM's specifications, it expresses the input constraints $S(.)$, which is important for the motor, meaning the control inputs i_q^*, u_d, and u_q are unable to be applied directly to the each subsystem, which will be defined later in (35) and (36).

The first subsystem is based on the dynamic of the EMLA, representing the linear position and velocity in (24), and current-q control i_q^*, is proposed to control the position and velocity. The second subsystem exploits the voltage-d control (u_d) for (22), after receiving the i_q^* control value from the previous subsystem, to force the states i_d and $\dot{i}_d$ to track the $i_d^*(= 0)$, according to Park's concept. Finally, the last subsystem determines the voltage-q control (u_q) for (22) to force the real i_q and $\dot{i}_q$ to track i_q^* and $\dot{i}_q^*$ received from the first subsystem as the reference value. Because the RDSC uses the model-based EMLA, it must be robust enough against nonlinear load effects and modelling errors. In this process, the RDSC, which requires only reference trajectories and real state values, can sufficiently produce the voltages and currents to tolerate a high load and uncertainties. For more details, the interconnection between subsystems of the RDSC structure regarding the EMLA has been illustrated in Fig. 2. Before investigating each subsystem analysis separately, we must provide some definitions, as follows.

Definition (1): assuming the function a_k values for $k = 1, ..., 5$ are virtual controls and differentiable, we define the following function to reduce the backstepping complexity and uncertainties, as follows:

$$\begin{aligned}
&\overline{F}_1 = F_1(x_1) \\
&\overline{F}_2 = F_2(x_1, x_2) - \frac{\partial a_1}{\partial x_1}\frac{\mathrm{d}x_1}{\mathrm{d}t} - \frac{\partial a_1}{\partial \hat{\theta}_1}\frac{\mathrm{d}\hat{\theta}_1}{\mathrm{d}t} \\
&\overline{F}_3 = F_3(x_1, ..., x_3) \\
&\overline{F}_4 = F_4(x_1, ..., x_4) - \frac{\partial a_3}{\partial x_3}\frac{\mathrm{d}x_3}{\mathrm{d}t} - \frac{\partial a_3}{\partial \hat{\theta}_3}\frac{\mathrm{d}\hat{\theta}_3}{\mathrm{d}t} \\
&\overline{F}_5 = F_5(x_1, ..., x_5) \\
&\overline{F}_6 = F_6(x_1, ..., x_6) - \frac{\partial a_5}{\partial x_5}\frac{\mathrm{d}x_5}{\mathrm{d}t} - \frac{\partial a_5}{\partial \hat{\theta}_5}\frac{\mathrm{d}\hat{\theta}_5}{\mathrm{d}t}
\end{aligned} \tag{31}$$

where $a_0 = a_2 = a_4 = 0$. By assuming that there is a positive constant Λ, and a smooth function r, which is assumed always within the upper bound of uncertainties, d_{max}, as the bound of external disturbances, and a positive parameter Ω, which all can be unknown, we can define:

$$\begin{aligned}
&| \overline{F}_k | \leq \Lambda_k r_k \ , \ \ | d_k | \leq d_{max(k)} \quad \Rightarrow \ k = 1, ..., 6 \\
&| \ddot{x}_d | \leq \Omega
\end{aligned} \tag{32}$$

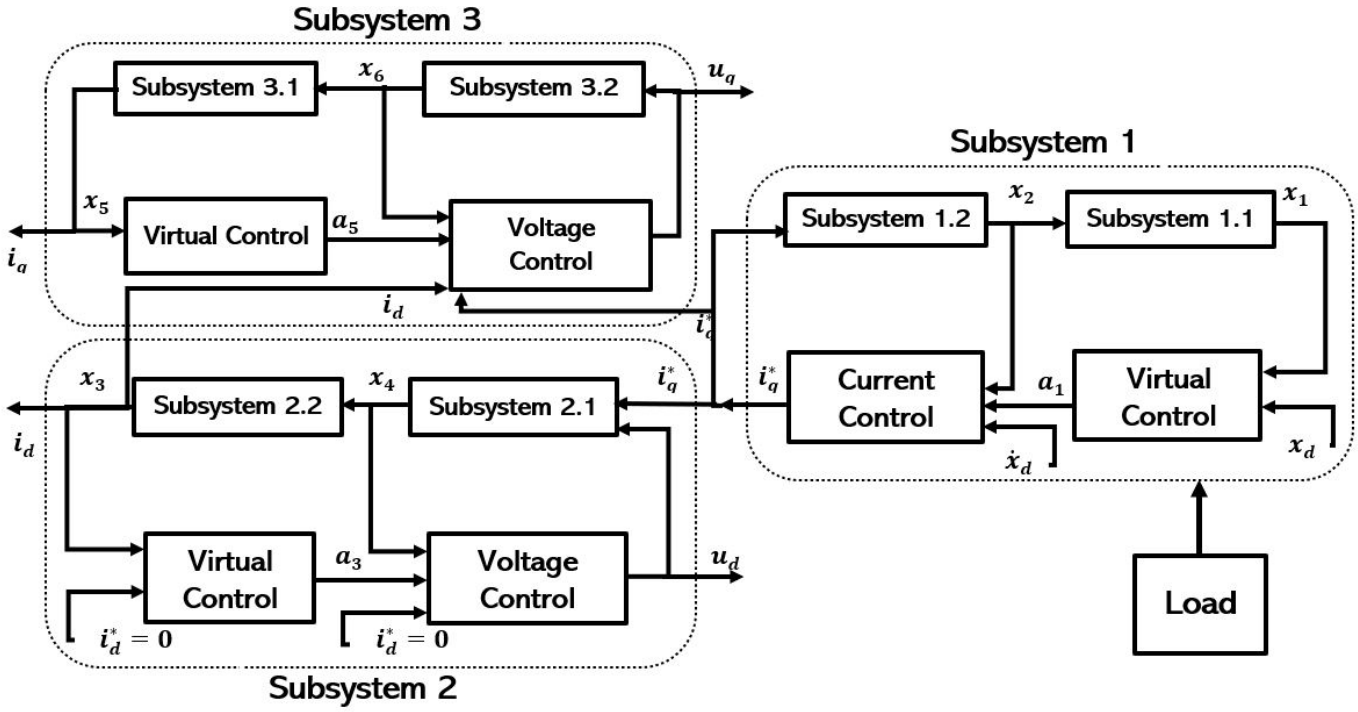

FIGURE 2 The control structure.

Where x_d can be the reference value of the states x_1, x_3, and x_5. To consider a robust adaptive law, we define the functions for subsystems to compensate for estimation errors, as follows:

$$\begin{aligned}
&\frac{1}{2}\zeta_1\theta_1^* = \frac{1}{2} + \mu_1\lambda_{min}\Lambda_1^2 + \nu_1\lambda_{min}d_{max(1)}^2 \\
&\frac{1}{2}\lambda_{min}\zeta_2\theta_2^* = \frac{1}{2}\lambda_{min} + \mu_2\Lambda_2^2 + \nu_2 d_{max(2)}^2 + \nu_3(\Omega)^2 + \nu_4\left(g_2\bar{\lambda}_{\max}\right)^2 \\
&\frac{1}{2}\zeta_3\theta_3^* = \frac{1}{2} + \mu_3\lambda_{min}\Lambda_3^2 + \nu_5\lambda_{min}d_{max(3)}^2 \\
&\frac{1}{2}\lambda_{min}\zeta_4\theta_4^* = \frac{1}{2}\lambda_{min} + \mu_4\Lambda_4^2 + \nu_6 d_{max(4)}^2 + \nu_7\left(g_4\bar{\lambda}_{\max}\right)^2 \\
&\frac{1}{2}\zeta_5\theta_5^* = \frac{1}{2} + \mu_5\lambda_{min}\Lambda_5^2 + \nu_8\lambda_{min}d_{max(5)}^2 \\
&\frac{1}{2}\lambda_{min}\zeta_6\theta_6^* = \frac{1}{2}\lambda_{min} + \mu_6\Lambda_6^2 + \nu_9 d_{max(6)}^2 + \nu_{10}(\Omega)^2 + \nu_{11}\left(g_6\bar{\lambda}_{\max}\right)^2
\end{aligned} \tag{33}$$

All parameters are assumed positive and will be defined later, and they can be unknown except ζ_k for $k = 1, ..., 6$, which will be used as a control design parameter. θ_k^* is a finite function to adjust the adaptive estimation, and it is also unknown.

Definition (2): Uniform exponential stability is a property of dynamical systems that ensures system solutions decay exponentially at a uniform rate. More formally, a dynamical system is said to be uniformly exponentially stable if there exist positive constants α and c, such that for any initial condition $x(0)$, and positive $\tilde{\mu}$, the distance between their trajectories decays exponentially at a uniform rate:

$$\|x(t) - x_d(t)\| \leq ce^{-\alpha t}\|x(0)\| + \tilde{\mu} \tag{34}$$

where $\|\cdot\|$ denotes a norm on the state space of the system, and $t \geq 0$ is the time variable. Uniform exponential stability is an important concept in the field of control theory, referring to a property of a dynamical system where, for any initial condition, the system's response converges exponentially fast to an equilibrium point, and the rate of convergence is independent of the initial condition.

Definition (3): As mentioned earlier in (30), it is mandatory to consider control input constraints in the EMLA application.

In this way, S(u(t)), as a function of the constraints on the control inputs, is defined as follows:

$$S(u(t)) = \begin{cases} u_1, & \text{if } u(t) \geq u_1 \\ u(t) & \text{if } u_1 \leq u(t) \leq u_2 \\ u_2 & \text{if } u(t) \leq u_2 \end{cases} \tag{35}$$

where u_1 and u_2 are the high and low bound values of $u(t)$. To a greater extent:

$$\boxed{S(u(t)) = \lambda_i \; u(t) + \bar{\lambda}_i \;\Rightarrow\; i = 1, 2, 3 \;\text{ specifying the number of subsystems.}} \tag{36}$$

where

$$\lambda_i = \begin{cases} \frac{1}{|u(t)|+1}, & \text{if} \quad u(t) \geq u_1 \quad \text{or} \quad u(t) \leq u_2 \\ 1 & \text{if} \quad u_1 \leq u(t) \leq u_2 \end{cases} \tag{37}$$

and

$$\bar{\lambda}_i = \begin{cases} u_1 - \frac{u(t)}{|u(t)|+1}, & \text{if } u(t) \geq u_1 \\ 0 & \text{if } u_1 \leq u(t) \leq u_2 \\ u_2 - \frac{u(t)}{|u(t)|+1} & \text{if } u(t) \leq u_2 \end{cases} \tag{38}$$

As we can see, $\bar{\lambda}_i \leq \max(\mid u_1 \mid +1, \; \mid u_2 \mid +1) = \bar{\lambda}_{max}$, and $\lambda_i \leq 1$, and we can define $0 \leq \lambda_{min} = \inf(\lambda_i)$, which were expressed before in (33).

Assumption (1): It is assumed that all states of the system are known and differentiable.

Assumption (2): It is assumed that external disturbances, and uncertainties are unknown and bounded. Except for the upper and lower constraints of control input (u_1 and u_2) based on the EMLA specification, we assume that we do not require any more knowledge about input saturation.

In the following, the RDSC for the EMLA system, expressed in section 2, will be defined, and a stability analysis will be conducted.

4 | EMLA CONTROL BASED ON RDSC

As expressed in section 3, in each subsystem, we have two sub-subsystems, the first of which is controlled by the virtual control a_k, which expressed in (31), and the second is controlled by factual control law. Now, we introduce the virtual control for each subsystem, as follows:

$$\boxed{\begin{array}{lll} \textbf{Subsystem 1} \;\Rightarrow & a_0 = 0\;, & a_1 = -\frac{1}{2}(\beta_1 + \zeta_1 \hat{\theta}_1) P_1 \\ \cdots\cdots\cdots\cdots & & \\ \textbf{Subsystem 2} \;\Rightarrow & a_2 = 0\;, & a_3 = -\frac{1}{2}(\beta_3 + \zeta_3 \hat{\theta}_3) P_3 \\ \cdots\cdots\cdots\cdots & & \\ \textbf{Subsystem 3} \;\Rightarrow & a_4 = 0\;, & a_5 = -\frac{1}{2}(\beta_5 + \zeta_5 \hat{\theta}_5) P_5 \end{array}} \tag{39}$$

Similar to (39), by knowing $g_2, g_4, and g_6$, as the factors of the control inputs, are non-zero, the current-q, voltage-d, and voltage-q control for the three subsystems can be proposed as follows:

$$\boxed{\begin{array}{ll} \textbf{Subsystem 1} \;\Rightarrow & i_q^* = \frac{-1}{2g_2}(\beta_2 + \zeta_2 \hat{\theta}_2) P_2 \\ \cdots\cdots\cdots\cdots & \\ \textbf{Subsystem 2} \;\Rightarrow & u_d = \frac{-1}{2g_4}(\beta_4 + \zeta_4 \hat{\theta}_4) P_4 \\ \cdots\cdots\cdots\cdots & \\ \textbf{Subsystem 3} \;\Rightarrow & u_q = \frac{-1}{2g_6}(\beta_6 + \zeta_6 \hat{\theta}_6) P_6 \end{array}} \tag{40}$$

where for $k = 1, ..., 6$, ζ_k follows (33), and β_k are positive constants, and $P_k = \bar{x}_k - a_{k-1}$, which $\bar{x}_k$ will be introduced later. $\hat{\theta}_k$, an adaptive function that can compensate for unknown effects that are imposed both outside and inside of the system, is introduced

for all six sub-subsystems as follows:

$$\boxed{\dot{\hat{\theta}}_k = -\delta_k \sigma_k \hat{\theta}_k + \frac{1}{2}\zeta_k \delta_k |P_k|^2 \;\Rightarrow\; k = 1, ..., 6} \tag{41}$$

where δ_k and σ_k are assumed positive parameters. As mentioned earlier, the RDSC has a straightforward form and only requires a simple mathematical, which showed in (39), (40), and (41).

Assumption 3: Assuming, for $k = 2, 4, 6$, $\hat{\theta}_k(0) > 0$, we can establish the following guarantee: for all $t \geq 0$, if the system evolves according to the dynamics that govern $\hat{\theta}_k(t)$, then $\hat{\theta}_k(t) \geq 0$.

By defining the adaptation error $\tilde{\theta}_k = \hat{\theta}_k - \theta_k^*$ and inserting it into (41), we have:

$$\dot{\tilde{\theta}}_k = -\delta_k \sigma_k \tilde{\theta}_k + \frac{1}{2}\zeta_k \delta_k |P_k|^2 - \delta_k \sigma_k \theta_k^* \tag{42}$$

where θ_k^* follows (33) to tune the adaptation law and compensate for the load effect, and uncertainties are unknown. The implementation of the proposed control approach, illustrated in Figure 2, in the EMLA system, allows a schematic representation of the RDSC for EMLA as observed in Figure 3. After obtaining the desired trajectories from the motion profile of the EMLA and retrieving the immediate states of the EMLA from the state detection section, the RDSC generates the necessary command voltages for the PMSM, similar to Fig. 1 illustrated by Chai, et al. in[44].

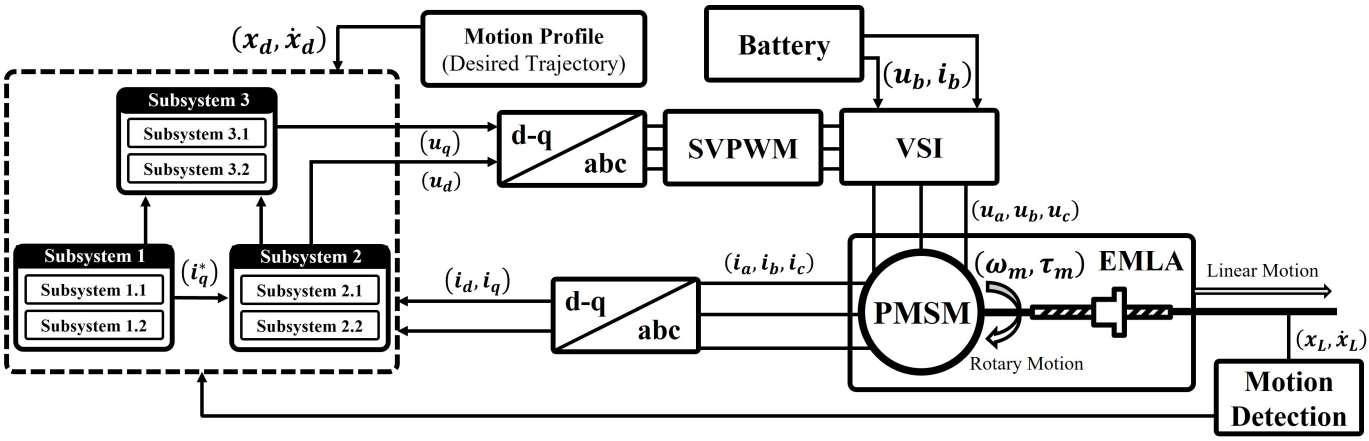

FIGURE 3 Schemtic of the proposed controller for the EMLA

Remark 1: We defined many parameters, although most are considered for the stability analysis and can be unknown. Thus, only few parameters will be used in the RDSC including β, ζ, δ, and σ as the control design parameters, which bring a straightforward control form.

Theorem (1): Regarding the issue of enough robustness to force states to track the desired trajectory of the EMLA with unknown external disturbances and uncertainties, and considering the control input constraints expressed in (35), we claim that all states provided in all three subsystems by following the RDSC satisfy the tracking process of the model, and are uniformly exponentially bounded, which expressed in Definition (2).

Now, we aim to investigate each subsystem via stability analysis and Theorem 1 proof separately, although the methods for each are highly similar.

4.1 | Current control-q stability (subsystem 1)

Following the previous section, we can define the first subsystem of the EMLA, according to (24) and (30), as follows:

$$\boxed{\begin{aligned} \dot{x}_1 &= x_2 + F_1(x_1) + d_1 \\ \dot{x}_2 &= g_2 S(i_q^*) + F_2(x_1, x_2) + d_2 \end{aligned}} \tag{43}$$

where $x_1 = x_L$ immediate linear position, $x_2 = \dot{x}_L$ immediate linear velocity, $F_1(x_1) = f_1$ is the unknown uncertainties, $g_2 = \frac{3}{2} I_{eq}^{-1} P \psi_{PM}$, $F_2 = -I_{eq}^{-1}(b_{eq} x_2 + k_{eq} x_1) + f_2$ is the uncertainties, and d_1 and d_2 are load disturbances. In this way, we define the error of tracking as follows:

$$\begin{aligned} \overline{x}_1 &= x_1 - x_d \\ \overline{x}_2 &= x_2 - \dot{x}_d \end{aligned} \tag{44}$$

where x_d and $\dot{x}_d$ are the reference trajectories for the linear position and velocity, respectively. We alter the form of the system to the tracking form as shown:[45]

$$\begin{aligned} P_1 &= \overline{x}_1 \\ P_2 &= \overline{x}_2 - a_1 \end{aligned} \tag{45}$$

where a_1 is a virtual control for sub-subsystem 1 introduced in (39). To avoid the "explosion of the complexity", derived from Wang, et al.,[28] the time derivative of the virtual control input is treated as an uncertain term in the system, according to (39). In this way, by differentiating (45) and inserting (43) and (44) into it, we will have a new form of the first subsystem, as follows:

$$\begin{aligned} \dot{P}_1 &= P_2 + \overline{F}_1 + a_1 + d_1 \\ \dot{P}_2 &= g_2 S(i_q^*) + \overline{F}_2 - \ddot{x}_d + d_2 \end{aligned} \tag{46}$$

and i_q^* is the current-q control in the first subsystem. In addition, the current-q control constraint derived from (35) is introduced as follows:

$$S(i_q^*) = \begin{cases} i_{q1}^*, & \text{if } i_q^* \geq i_{q1}^* \\ i_q^* & \text{if } i_{q2}^* \leq i_q^* \leq i_{q1}^* \\ i_{q2}^* & \text{if } i_q^* \leq i_{q2}^* \end{cases} \tag{47}$$

The Lyapunov function for the first sub-subsystem are suggested as follows:

$$V_1 = \frac{1}{2}\ \lambda_{min}[{P_1}^2 + \delta_1^{-1}\tilde{\theta}_1^2] \tag{48}$$

After differentiating V_1 and inserting (46), we obtain:

$$\dot{V}_1 = P_1 \lambda_{min}[P_2 + \overline{F}_1 + a_1 + d_1] + \delta_1^{-1}\lambda_{min}\tilde{\theta}_1\dot{\tilde{\theta}}_1 \tag{49}$$

After conducting simple mathematical work, we obtain:

$$\dot{V}_1 = \lambda_{min} P_1 P_2 + \lambda_{min} P_1 \overline{F}_1 + \lambda_{min} P_1 d_1 + \lambda_{min} P_1 a_1 + \delta_1^{-1}\lambda_{min}\tilde{\theta}_1\dot{\tilde{\theta}}_1 \tag{50}$$

By considering (32), we have:

$$\dot{V}_1 \leq \lambda_{min} P_1 P_2 + \lambda_{min} \mid P_1 \mid \Lambda_1 r_1 + \lambda_{min} \mid P_1 \mid d_{max(1)} + \lambda_{min} P_1 a_1 + \delta_1^{-1}\lambda_{min}\tilde{\theta}_1\dot{\tilde{\theta}}_1 \tag{51}$$

By using the mathematical concept $(P_1 - P_2)^2 \geq 0$, we obtain

$$\dot{V}_1 \leq \frac{1}{2}\lambda_{min} P_1^2 + \frac{1}{2}\lambda_{min} P_2^2 + \lambda_{min} \mid P_1 \mid \Lambda_1 r_1 + \lambda_{min} \mid P_1 \mid d_{max(1)} + \lambda_{min} P_1 a_1 + \delta_1^{-1}\lambda_{min}\tilde{\theta}_1\dot{\tilde{\theta}}_1 \tag{52}$$

Because $\Lambda_1 r_1$ and $d_{max(1)}$ are meant to be finite, we can assume positive values for ν_1, and μ_1, as follows:

$$\begin{aligned} \lambda_{min} \mid P_1 \mid \Lambda_1 r_1 &\leq \mu_1 \lambda_{min}^2 \mid P_1 \mid^2 \Lambda_1^2 + \frac{1}{4}\mu_1^{-1} r_1^2 \\ \lambda_{min} \mid P_1 \mid d_{max(1)} &\leq \nu_1 \lambda_{min}^2 \mid P_1 \mid^2 d_{max(1)}^2 + \frac{1}{4}\nu_1^{-1} \end{aligned} \tag{53}$$

Then, by considering the definition of θ_1^* in (33) and the definition of (53), we achieve:

$$\dot{V}_1 \leq \frac{1}{2}\lambda_{min} P_2^2 + \frac{1}{2}\lambda_{min}\zeta_1\theta_1^* \mid P_1 \mid^2 + \frac{1}{4}\mu_1^{-1} r_1^2 + \frac{1}{4}\nu_1^{-1} + \lambda_{min} P_1 a_1 + \delta^{-1}\lambda_{min}\tilde{\theta}_1\dot{\tilde{\theta}}_1 \tag{54}$$

Now, by inserting (39) and (42), we have:

$$\begin{aligned} \dot{V}_1 \leq & \frac{1}{2}\lambda_{min} P_2^2 + \frac{1}{2}\lambda_{min}\zeta_1\theta_1^* \mid P_1 \mid^2 + \frac{1}{4}\mu_1^{-1} r_1^2 + \frac{1}{4}\nu_1^{-1} - \frac{1}{2}\lambda_{min}\beta_1 P_1^2 - \frac{1}{2}\lambda_{min}\zeta_1\hat{\theta}_1 P_1^2 \\ & - \lambda_{min}\sigma_1\tilde{\theta}_1^2 + \frac{1}{2}\lambda_{min}\zeta_1 |P_1|^2\tilde{\theta}_1 - \lambda_{min}\sigma_1\theta_1^*\tilde{\theta}_1 \end{aligned} \tag{55}$$

Because $\tilde{\theta}_1 = \hat{\theta}_1 - \theta_1^*$:

$$\dot{V}_1 \leq \frac{1}{2}\lambda_{min} P_2^2 + \frac{1}{4}\mu_1^{-1} r_1^2 + \frac{1}{4}\nu_1^{-1} - \frac{1}{2}\lambda_{min}\beta_1 P_1^2 - \lambda_{min}\sigma_1\tilde{\theta}_1^2 - \lambda_{min}\sigma_1\theta_1^*\tilde{\theta}_1 \tag{56}$$

After dividing $\lambda_{min}\sigma_1\tilde{\theta}_1^2$ into $\frac{1}{2}\lambda_{min}\sigma_1\tilde{\theta}_1^2 + \frac{1}{2}\lambda_{min}\sigma_1\tilde{\theta}_1^2$, and considering (48), we have:

$$\dot{V}_1 \leq -\phi_1 V_1 + \frac{1}{2}\lambda_{min}P_2^2 + \frac{1}{4}\mu_1^{-1}r_1^2 + \frac{1}{4}\nu_1^{-1} - \frac{1}{2}\lambda_{min}\sigma_1\tilde{\theta}_1^2 - \lambda_{min}\sigma_1\theta_1^*\tilde{\theta}_1 \tag{57}$$

where

$$\phi_1 = \min[\beta_1, \quad \delta_1\sigma_1] \tag{58}$$

From (57), we have:

$$\dot{V}_1 \leq -\phi_1 V_1 + \frac{1}{2}\lambda_{min}P_2^2 + \frac{1}{4}\mu_1^{-1}r_1^2 + \frac{1}{4}\nu_1^{-1} - \frac{1}{2}\lambda_{min}\sigma_1(\hat{\theta}_1 - \theta_1^*)^2 - \lambda_{min}\sigma_1\theta_1^*(\hat{\theta}_1 - \theta_1^*) \tag{59}$$

Because $-\frac{1}{2}\lambda_{min}\sigma_1\hat{\theta}_1^2 \leq 0$, we can eliminate this part from the right side and reach:

$$\dot{V}_1 \leq -\phi_1 V_1 + \frac{1}{2}\lambda_{min}P_2^2 + \frac{1}{4}\mu_1^{-1}r_1^2 + \frac{1}{4}\nu_1^{-1} + \frac{1}{2}\lambda_{min}\sigma_1\theta_1^{*2} \tag{60}$$

Later, we will return to the stability of P_1. Now, we continue the stability proof for the second sub-subsystem, which implies the stability of the entire subsystem 1. Similar to the previous sub-subsystem, we can provide the same proof for the second sub-subsystem by defining the Lyapunov function as follows:

$$V_2 = V_1 + \frac{1}{2}\left[P_2^2 + \delta^{-1}\lambda_{min}\tilde{\theta}_2^2\right] \tag{61}$$

where V_1 is the Lyapunov function introduced for sub-subsystem 1 in (48). By differentiating V_2 and inserting (46), we have:

$$\dot{V}_2 = \dot{V}_1 + P_2[g_2 S(i_q^*) + \overline{F}_2 - \ddot{x}_d + d_2] + \delta_2^{-1}\lambda_{min}\tilde{\theta}_2\dot{\tilde{\theta}}_2 \tag{62}$$

Likewise, we continue by considering (60), inserted into (62) as follows:

$$\begin{aligned}\dot{V}_2 \leq & -\phi_1 V_1 + \frac{1}{2}\lambda_{min}P_2^2 + \frac{1}{4}\mu_1^{-1}r_1^2 + \frac{1}{4}\nu_1^{-1} + \frac{1}{2}\lambda_{min}\sigma_1\theta_1^{*2} \\ & + P_2 g_2 S(i_q^*) + P_2\overline{F}_2 - P_2\ddot{x}_d + P_2 d_2 + \delta_2^{-1}\lambda_{min}\tilde{\theta}_2\dot{\tilde{\theta}}_2\end{aligned} \tag{63}$$

By inserting (36) into (63), we have:

$$\begin{aligned}\dot{V}_2 \leq & -\phi_1 V_1 + \frac{1}{2}\lambda_{min}P_2^2 + \frac{1}{4}\mu_1^{-1}r_1^2 + \frac{1}{4}\nu_1^{-1} + \frac{1}{2}\lambda_{min}\sigma_1\theta_1^{*2} \\ & + P_2 g_2\lambda_1\, i_q^* + P_2 g_2\bar{\lambda}_1 + P_2\overline{F}_2 - P_2\ddot{x}_d + P_2 d_2 + \delta_2^{-1}\lambda_{min}\tilde{\theta}_2\dot{\tilde{\theta}}_2\end{aligned} \tag{64}$$

By inserting current-q control i_q^* inserted from (40) into (64)

$$\begin{aligned}\dot{V}_2 \leq & -\phi_1 V_1 + \frac{1}{2}\lambda_{min}P_2^2 + \frac{1}{4}\mu_1^{-1}r_1^2 + \frac{1}{4}\nu_1^{-1} + \frac{1}{2}\lambda_{min}\sigma_1\theta_1^{*2} - \frac{1}{2}\lambda_1\beta_2 {P_2}^2 \\ & - \frac{1}{2}\lambda_1\zeta_2\hat{\theta}_2 {P_2}^2 + P_2 g_2\bar{\lambda}_1 + P_2\overline{F}_2 - P_2\ddot{x}_d + P_2 d_2 + \delta_2^{-1}\lambda_{min}\tilde{\theta}_2\dot{\tilde{\theta}}_2\end{aligned} \tag{65}$$

By considering $\hat{\theta}_2(0) \geq 0$ according to assumption 3, and because $\lambda_{min}, \lambda_1 \geq 0$, and $\lambda_{min} \leq \lambda_1$, we can say:

$$\begin{aligned}\dot{V}_2 \leq & -\phi_1 V_1 + \frac{1}{2}\lambda_{min}P_2^2 + \frac{1}{4}\mu_1^{-1}r_1^2 + \frac{1}{4}\nu_1^{-1} + \frac{1}{2}\lambda_{min}\sigma_1\theta_1^{*2} - \frac{1}{2}\lambda_{min}\beta_2 {P_2}^2 \\ & - \frac{1}{2}\lambda_{min}\zeta_2\hat{\theta}_2 {P_2}^2 + P_2 g_2\bar{\lambda}_1 + P_2\overline{F}_2 - P_2\ddot{x}_d + P_2 d_2 + \delta_2^{-1}\lambda_{min}\tilde{\theta}_2\dot{\tilde{\theta}}_2\end{aligned} \tag{66}$$

Similar to (53), by knowing (32) and (38), we can assume:

$$\begin{aligned}P_2\overline{F}_2 &\leq \mu_2\Lambda_2^2 P_2^2 + \frac{1}{4}\mu_2^{-1}r_2^2 \\ P_2 d_2 &\leq \nu_2 d_{max2}^2 P_2^2 + \frac{1}{4}\nu_2^{-1} \\ -P_2\ddot{x}_d &\leq \nu_3\Omega^2 P_2^2 + \frac{1}{4}\nu_3^{-1} \\ P_2 g_2\bar{\lambda}_1 &\leq \nu_4 g_2^2\bar{\lambda}_{max}^2 P_2^2 + \frac{1}{4}\nu_4^{-1}\end{aligned} \tag{67}$$

where we have:

$$\begin{aligned}\dot{V}_2 \leq & -\phi_1 V_1 + \frac{1}{2}\lambda_{min} P_2^2 + \frac{1}{4}\sum_{i=1}^{2}\mu_i^{-1} r_i^2 + \frac{1}{4}\sum_{i=1}^{4}\nu_i^{-1} + \frac{1}{2}\lambda_{min}\sigma_1\theta_1^{*2} - \frac{1}{2}\lambda_{min}\beta_2 {P_2}^2 \\ & - \frac{1}{2}\lambda_{min}\zeta_2\hat{\theta}_2 {P_2}^2 + \nu_4 g_2^2 \bar{\lambda}_{max}^2 P_2^2 + \mu_2 \Lambda_2^2 P_2^2 + \nu_3 \Omega^2 P_2^2 + \nu_2 d_{max2}^2 P_2^2 + \delta_2^{-1}\lambda_{min}\tilde{\theta}_2\dot{\tilde{\theta}}_2\end{aligned} \tag{68}$$

By considering θ_2^* in (33):

$$\begin{aligned}\dot{V}_2 \leq & -\phi_1 V_1 + \frac{1}{4}\sum_{i=1}^{2}\mu_i^{-1} r_i^2 + \frac{1}{4}\sum_{i=1}^{4}\nu_i^{-1} + \frac{1}{2}\lambda_{min}\sigma_1\theta_1^{*2} - \frac{1}{2}\lambda_{min}\beta_2 {P_2}^2 \\ & - \frac{1}{2}\lambda_{min}\zeta_2\hat{\theta}_2 {P_2}^2 + \frac{1}{2}\lambda_{min}\zeta_2\theta_2^* P_2^2 + \delta_2^{-1}\lambda_{min}\tilde{\theta}_2\dot{\tilde{\theta}}_2\end{aligned} \tag{69}$$

By inserting $\tilde{\theta}_2$ from (42) into (69):

$$\begin{aligned}\dot{V}_2 \leq & -\phi_1 V_1 + \frac{1}{4}\sum_{i=1}^{2}\mu_i^{-1} r_i^2 + \frac{1}{4}\sum_{i=1}^{4}\nu_i^{-1} + \frac{1}{2}\lambda_{min}\sigma_1\theta_1^{*2} - \frac{1}{2}\lambda_{min}\beta_2 {P_2}^2 \\ & - \frac{1}{2}\lambda_{min}\zeta_2\hat{\theta}_2 {P_2}^2 + \frac{1}{2}\lambda_{min}\zeta_2\theta_2^* P_2^2 - \lambda_{min}\sigma_2\tilde{\theta}_2^2 + \frac{1}{2}\lambda_{min}\zeta_2\tilde{\theta}_2 |P_2|^2 - \lambda_{min}\sigma_2\theta_2^*\tilde{\theta}_2\end{aligned} \tag{70}$$

Some mathematical works:

$$\dot{V}_2 \leq -\phi_1 V_1 + \frac{1}{4}\sum_{i=1}^{2}\mu_i^{-1} r_i^2 + \frac{1}{4}\sum_{i=1}^{4}\nu_i^{-1} + \frac{1}{2}\lambda_{min}\sigma_1\theta_1^{*2} - \frac{1}{2}\lambda_{min}\beta_2 {P_2}^2 - \lambda_{min}\sigma_2\tilde{\theta}_2^2 - \lambda_{min}\sigma_2\theta_2^*\tilde{\theta}_2 \tag{71}$$

By dividing $-\lambda_{min}\sigma_2\tilde{\theta}_2^2$, knowing (61), and noting that $0 \leq \lambda_{min} \leq 1$:

$$\dot{V}_2 \leq -\phi_2 V_2 + \frac{1}{4}\sum_{i=1}^{2}\mu_i^{-1} r_i^2 + \frac{1}{4}\sum_{i=1}^{4}\nu_i^{-1} + \frac{1}{2}\sum_{i=1}^{2}\lambda_{min}\sigma_i\theta_i^{*2} \tag{72}$$

where

$$\phi_2 = \min[\phi_1, \quad \beta_2, \quad \delta_2\sigma_2] \tag{73}$$

For brevity, we introduce:

$$\tilde{\mu}_2 = \frac{1}{2}\sum_{i=1}^{2}\lambda_{min}\sigma_i\theta_i^{*2} + \frac{1}{4}\sum_{i=1}^{4}\nu_i^{-1} \tag{74}$$

Thus,

$$\dot{V}_2 \leq -\phi_2 V_2 + \frac{1}{4}\sum_{i=1}^{2}\mu_i^{-1} r_i^2 + \tilde{\mu}_2 \tag{75}$$

Taken from the general solution for state-space representation, we can say:

$$\dot{V} = \phi V + \mu r \quad \Rightarrow \quad V = e^{\phi t} V(0) + \int_0^t e^{\phi(t-\tau)}\mu r(\tau) d\tau \tag{76}$$

Thus, we can solve (75), as follows:

$$V_2 \leq V_2\left(t_0\right) e^{-\{\phi_2(t-t_0)\}} + \frac{1}{4}\sum_{i=1}^{2}\mu_i^{-1}\int_{t_0}^{t} e^{\{-\phi_2(t-T)\}} r_i^2 \; dT + \tilde{\mu}_2 \int_{t_0}^{t} e^{\{-\phi_2(t-T)\}} \; dT \tag{77}$$

Regarding (61), we can interpret (77) as follows:

$$\|P_2\|^2 \leq 2V_2\left(t_0\right) e^{-\{\phi_2(t-t_0)\}} + \frac{1}{2}\sum_{i=1}^{2}\mu_i^{-1}\int_{t_0}^{t} e^{\{-\phi_2(t-T)\}} r_i^2 \; dT + 2\;\tilde{\mu}_2\;{\phi_2}^{-1} \tag{78}$$

Because μ_i is a positive constant, we can express that:

$$\frac{1}{2}\sum_{i=1}^{2}\frac{1}{\mu_i\phi_2} < 1 \tag{79}$$

Hence, a continuous function can be assumed as follows:

$$Z(\iota) = \frac{1}{2}\sum_{i=1}^{2}\frac{\mu_i^{-1}}{\phi_2 - \iota} > 0 \;\Rightarrow\; \boxed{\iota \in [0, \phi_2)} \tag{80}$$

Notice that the initial amount in (80) equals (79). Now, it is obvious to say that there is a positive amount $\bar{\iota} \in \iota$, such that:

$$0 \leq \bar{Z} = Z(\bar{\iota}) < 1 \tag{81}$$

By multiplying $e^{\bar{\iota}(t-t_0)}$ by (78), we reach:

$$\|P_2\|^2 e^{\bar{\iota}(t-t_0)} \leq 2V_2(t_0)e^{-(\phi_2-\bar{\iota})(t-t_0)} + \frac{1}{2}\sum_{i=1}^{2}\mu_i^{-1}\int_{t_0}^{t} e^{-\phi_2(t-T)+\bar{\iota}(t-t_0)} r_i^2 \; dT + 2\tilde{\mu}_2\phi_2^{-1}e^{\bar{\iota}(t-t_0)} \tag{82}$$

Because $0 \leq \bar{\iota} < \phi_2$, we can eliminate the decreasing element $e^{-(\phi_2-\bar{\iota})(t-t_0)}$ from the right side of the inequality in (82):

$$\|P_2\|^2 e^{\bar{\iota}(t-t_0)} \leq 2V_2(t_0) + \frac{1}{2}\sum_{i=1}^{2}\mu_i^{-1}\int_{t_0}^{t} e^{-(\phi_2-\bar{\iota})(t-T)} r_i^2 e^{\bar{\iota}(t-t_0)} \; dT + 2\tilde{\mu}_2\phi_2^{-1}e^{\bar{\iota}(t-t_0)} \tag{83}$$

In this way, we can express the continuous and non-decreasing functions E_0 and E_i:

$$\begin{aligned} E_0 &= \sup_{e\in(t-t_0)} [\|P_2\|^2 e^{\bar{\iota}(e-t_0))}] \\ E_i &= \sup_{e\in(t-t_0)} [(r_i^2)e^{\bar{\iota}(e-t_0)}] \end{aligned} \tag{84}$$

Then, by considering (84) and performing some simple mathematical works, as well as eliminating the negative section, we have:

$$\|P_2\|^2 e^{\bar{\iota}(t-t_0)} \leq 2V_2(t_0) + \frac{1}{2}\sum_{i=1}^{2}\frac{\mu_i^{-1}}{\phi_2 - \bar{\iota}}E_i + 2\tilde{\mu}_2\phi_2^{-1}e^{\bar{\iota}(t-t_0)} \tag{85}$$

Because E_i is not decreasing, the left side of (85) will not decrease. Therefore, regarding the definition of E_0 in (84), we can say

$$E_0 \leq 2V_2(t_0) + \frac{1}{2}\sum_{i=1}^{2}\frac{\mu_i^{-1}}{\phi_2 - \bar{\iota}}E_i + 2\tilde{\mu}_2\phi_2^{-1}e^{\bar{\iota}(t-t_0)} \tag{86}$$

By defining

$$E = \max_i (E_i) \;\Rightarrow\; \quad i = 0, 1, 2 \tag{87}$$

we can have:

$$E_0 \leq 2V_2\left(t_0\right) + \bar{Z}E + 2\tilde{\mu}_2\phi_2^{-1}e^{\bar{\iota}(t-t_0)} \tag{88}$$

that $0 < E_0 \leq E$ and both E_0 and E are not decreasing, allowing to define $\overset{*}{Z}$ as follows:

$$\overset{*}{Z} > \bar{Z} \;\;,\;\; 0 < \overset{*}{Z} < 1 \;\Rightarrow\; \bar{Z}E \leq \overset{*}{Z}E_0 \tag{89}$$

(89) makes sense because μ_i can be an option to make $\bar{Z}$ small enough. Adding (89) into (88), we reach:

$$E_0 \leq 2V_2(t_0) + \overset{*}{Z}E_0(t) + 2\tilde{\mu}_2\phi_2^{-1}e^{\bar{\iota}(t-t_0)} \tag{90}$$

Afterward, we obtain:

$$E_0 \leq \frac{2V_2\left(t_0\right) + 2\tilde{\mu}_2\phi_2^{-1}e^{\bar{\iota}(t-t_0)}}{1 - \overset{*}{Z}} \tag{91}$$

Concerning the definition (84), we obtain:

$$\|P_2\|^2 \leq \frac{2V_2\left(t_0\right)e^{-\bar{\iota}(t-t_0)} + 2\tilde{\mu}_2\phi_2^{-1}}{1 - \overset{*}{Z}} \tag{92}$$

It is significant that:

$$\sup_{t\in[t_0,\infty]}\left(\frac{2V_2(t_0)e^{-\bar{\iota}(t-t_0)}}{1 - \overset{*}{Z}}\right) \leq \frac{2V_2(t_0)}{1 - \overset{*}{Z}} \tag{93}$$

Thus, based on Definition (2), it is obvious from (92) that $\|P_2\|$ is uniformly exponentially bounded by using i_q^* control in (40). Therefore, $\|P_2\|$ will have uniform exponential stability inside to a specific ball $\mathcal{G}\left(\bar{\tau}_0\right)$, where:

$$\mathcal{G}\left(\bar{\tau}_0\right) := \left\{ P_2 \mid \|P_2\| \leq \bar{\tau}_0 = \sqrt{\frac{2\tilde{\mu}_2 \phi_2^{-1}}{1 - \overset{*}{Z}}} \right\} \tag{94}$$

By knowing that P_2 is uniformly exponential stable, we can return to (60) to continue the stability proof for the first sub-subsystem. Hence, we can introduce a finite positive value, as follows:

$$\tilde{\mu}_1 = \frac{1}{2}\lambda_{min} P_2^2 + \frac{1}{2}\lambda_{min}\sigma_1 \theta_1^{*2} + \frac{1}{4}\nu_1^{-1} \tag{95}$$

(95) makes sense because P_2 is uniformly exponential stable. Thus:

$$\dot{V}_1 \leq -\phi_1 V_1 + \frac{1}{4}\mu_1^{-1} r_1^2 + \tilde{\mu}_1 \tag{96}$$

Taken from the general solution for state-space representation, we can say:

$$\dot{V} = \phi V + \mu r \quad \Rightarrow \quad V = e^{\phi t} V(0) + \int_0^t e^{\phi(t-T)} \mu r(T) dT \tag{97}$$

Thus, we can solve (60) using (97) as follows:

$$V_1 \leq V_1\left(t_0\right) e^{-\{\phi_1(t-t_0)\}} + \frac{1}{4}\mu_1^{-1} \int_{t_0}^{t} e^{\{-\phi_1(t-T)\}} r_1^2 \; dT + \tilde{\mu}_1 \int_{t_0}^{t} e^{\{-\phi_1(t-T)\}} \; dT \tag{98}$$

regarding (48), and knowing $\lambda_{min} \leq 1$, we can interpret (98) as follows:

$$\|P_1\|^2 \leq 2V_1\left(t_0\right) e^{-\{\phi_1(t-t_0)\}} + \frac{1}{2}\mu_1^{-1} \int_{t_0}^{t} e^{\{-\phi_1(t-T)\}} r_1^2 \; dT + 2\;\tilde{\mu}_1\;{\phi_1}^{-1} \tag{99}$$

Because μ_1 is a positive constant, we assume that there is a μ_1 expressing:

$$\frac{1}{2}\left(\frac{1}{\mu_1 \phi_1}\right) < 1 \tag{100}$$

Hence, a continuous function can be defined as follows:

$$Z(\iota) = \frac{1}{2}\left(\frac{\mu_1^{-1}}{\phi_1 - \iota}\right) > 0 \;\Rightarrow\; \boxed{\iota \in [0, \phi_1)} \tag{101}$$

Notice that the initial amount in (101) is equal to (100). Now, it is obvious to say that there is a positive amount $\bar{\iota} \in \iota$, such that:

$$0 \leq \bar{Z} = Z(\bar{\iota}) < 1 \tag{102}$$

By multiplying $e^{\bar{\iota}(t-t_0)}$ by (99), we reach:

$$\|P_1\|^2 e^{\bar{\iota}(t-t_0)} \leq 2V_1(t_0) e^{-(\phi_1 - \bar{\iota})(t-t_0)} + \frac{1}{2}\mu_1^{-1} \int_{t_0}^{t} e^{-\phi_1(t-T)+\bar{\iota}(t-t_0)} r_1^2 \; dT + 2\tilde{\mu}_1 \phi_1^{-1} e^{\bar{\iota}(t-t_0)} \tag{103}$$

Because $0 \leq \bar{\iota} < \phi_1$ an $t \geq t_0$, we can eliminate the decreasing element $e^{-(\phi_1 - \bar{\iota})(t-t_0)}$ as the factor of $V_1(t_0)$ from the right side of the inequality in (103):

$$\|P_1\|^2 e^{\bar{\iota}(t-t_0)} \leq 2V_1(t_0) + \frac{1}{2}\mu_1^{-1} \int_{t_0}^{t} e^{-(\phi_1 - \bar{\iota})(t-T)} r_1^2 e^{\bar{\iota}(t-t_0)} \; dT \quad + 2\tilde{\mu}_1 \phi_1^{-1} e^{\bar{\iota}(t-t_0)} \tag{104}$$

In this way, we can express the continuous and non-decreasing functions E_0 and E_i:

$$\begin{aligned} E_0 &= \sup_{e \in (t-t_0)} \; [\|P_1\|^2 e^{\bar{\iota}(e-t_0))}] \\ E_1 &= \sup_{e \in (t-t_0)} \; [(r_1^2) e^{\bar{\iota}(e-t_0)}] \end{aligned} \tag{105}$$

Then, by considering (105) and performing some simple mathematical works, we have:

$$\|P_1\|^2 e^{\bar{\imath}(t-t_0)} \leq 2V_1(t_0) + \frac{1}{2}\frac{\mu_1^{-1}}{\phi_1 - \bar{\imath}}E_1 + 2\tilde{\mu}_2\phi_2^{-1}e^{\bar{\imath}(t-t_0)} \tag{106}$$

Because E_1 is not decreasing, the left side of (106) will not decrease. Therefore, regarding the definition of E_0 in (105), we can say:

$$E_0 \leq 2V_1(t_0) + \frac{1}{2}\frac{\mu_1^{-1}}{\phi_1 - \bar{\imath}}E_1 + 2\tilde{\mu}_1\phi_1^{-1}e^{\bar{\imath}(t-t_0)} \tag{107}$$

defining

$$E = \max_i (E_i) \Rightarrow \quad i = 0, 1 \tag{108}$$

After considering (101) and (102), we can have:

$$E_0 \leq 2V_1\left(t_0\right) + \bar{Z}E + 2\tilde{\mu}_1\phi_1^{-1}e^{\bar{\imath}(t-t_0)} \tag{109}$$

As with (108), we know that $0 < E_0 \leq E$ and both E_0 and E are not decreasing, allowing us to define $\overset{*}{Z}$ as follows:

$$\overset{*}{Z} > \bar{Z} \ , \ 0 < \overset{*}{Z} < 1 \xrightarrow{\text{such that}} \bar{Z}E \leq \overset{*}{Z}E_0 \tag{110}$$

(110) makes sense because μ_1 can be an option to make $\bar{Z}$ small enough. Adding (110) to (109), we reach:

$$E_0 \leq 2V_1(t_0) + \overset{*}{Z}E_0(t) + 2\tilde{\mu}_1\phi_1^{-1}e^{\bar{\imath}(t-t_0)} \tag{111}$$

Afterward, we obtain:

$$E_0 \leq \frac{2V_1\left(t_0\right) + 2\tilde{\mu}_1\phi_1^{-1}e^{\bar{\imath}(t-t_0)}}{1 - \overset{*}{Z}} \tag{112}$$

Concerning the definition (105), we obtain:

$$\|P_1\|^2 \leq \frac{2V_1\left(t_0\right)e^{-\bar{\imath}(t-t_0)} + 2\tilde{\mu}_1\phi_1^{-1}}{1 - \overset{*}{Z}} \tag{113}$$

It is significant that:

$$\sup_{t\in[t_0,\infty]} \left(\frac{2V_1(t_0)e^{-\bar{\imath}(t-t_0)}}{1 - \overset{*}{Z}}\right) \leq \frac{2V_1(t_0)}{1 - \overset{*}{Z}} \tag{114}$$

Thus, based on Definition (2), it is obvious from (113) and (114) that $\|P_1\|$ is uniformly exponentially bounded by use of the virtual control a_1 in (39). Therefore, $\|P_1\|$ will have uniform exponential stability inside to a specific ball $\mathcal{G}\left(\bar{\tau}_0\right)$, where:

$$\mathcal{G}\left(\bar{\tau}_0\right) := \left\{ P_1 \mid \|P_1\| \leq \bar{\tau}_0 = \sqrt{\frac{2\tilde{\mu}_1\phi_1^{-1}}{1 - \overset{*}{Z}}} \right\} \tag{115}$$

Finally, uniform exponential stability is fulfilled for the first sub-subsystem following Theorem (1).

4.2 | Voltage-d control stability (subsystem 2)

Similar to the first subsystem, the stability analysis of the second subsystem is as follows. Likewise, the second subsystem is introduced, according to (22), as follows:

$$\boxed{\begin{aligned} \dot{x}_3 &= x_4 + F_3(x_1, x_2, x_3) + d_3 \\ \dot{x}_4 &= g_4 S(u_d) + F_4(x_1, x_2, x_3, x_4) + d_4 \end{aligned}} \tag{116}$$

where $x_3 = i_d$, $x_4 = \dot{i}_d$ is the current-d and its derivative, $F_3 = f_3$, $g_4 = \frac{1}{L_d}$, $F_4 = \frac{-R_s}{L_d}x_3 + Pc_{RL}\frac{L_q}{L_d}i_q^* x_2 + f_4$ are uncertainties, d_3 and d_4 are external disturbances, and u_d is the voltage-d control in the second subsystem. According to (35), we have:

$$S(u_d) = \begin{cases} u_{d1}, & \text{if } u_d \geq u_{d1} \\ u_d & \text{if } u_{d2} \leq u_d \leq u_{d1} \\ u_{d2} & \text{if } u_d \leq u_{d2} \end{cases} \tag{117}$$

Similar to the previous subsystem, the two sub-subsystems should be controlled and analyzed as in (44). In this way, by defining the error of tracking as:

$$\begin{aligned} \overline{x}_3 &= x_3 - 0 \\ \overline{x}_4 &= x_4 - 0 \end{aligned} \tag{118}$$

in this subsystem, we consider that the reference values of both states are zero. We alter the form of the system to the tracking form, as shown[45]:

$$\begin{aligned} P_3 &= \overline{x}_3 \\ P_4 &= \overline{x}_4 - a_3 \end{aligned} \tag{119}$$

where a_3 is the virtual control for the second subsystem (sub-subsystem 1). To avoid the "explosion of the complexity" derived from Wang, et al.,[28] the time derivative of the virtual control input is treated as an uncertainty term in the system according to (39). By differentiating (119), we have:

$$\begin{aligned} \dot{P}_3 &= P_4 + \overline{F}_3 + a_3 + d_3 \\ \dot{P}_4 &= g_4 S(u_d) + \overline{F}_4 + d_4 \end{aligned} \tag{120}$$

The Lyapunov functions using the virtual control a_3 and the voltage-d control in (39) and (40) for the second subsystem are suggested as follows:

$$\begin{aligned} V_3 &= V_2 + \frac{1}{2}\lambda_{min}\left[{P_3}^2 + \delta_3^{-1}\tilde{\theta}_3^2\right] \\ V_4 &= V_3 + \frac{1}{2}\left[P_4^2 + \delta^{-1}\lambda_{min}\tilde{\theta}_4^2\right] \end{aligned} \tag{121}$$

All proof steps are the same as the previous subsystem provided in section 4.1, except that we consider the reference of states i_d^* and i_d^*, which are also zero. In this way, we have:

$$\begin{aligned} \lambda_{min}P_3\overline{F}_3 &\le \mu_3\lambda_{min}^2 \mid P_3 \mid^2 \Lambda_3^2 + \frac{1}{4}\mu_3^{-1}r_3^2 \\ \lambda_{min}P_3 d_3 &\le \nu_5\lambda_{min}^2 \mid P_3 \mid^2 d_{max(3)}^2 + \frac{1}{4}\nu_5^{-1} \\ P_4\overline{F}_4 &\le \mu_4\Lambda_4^2 P_4^2 + \frac{1}{4}\mu_4^{-1}r_4^2 \\ P_4 d_4 &\le \nu_6 d_{max(4)}^2 P_4^2 + \frac{1}{4}\nu_6^{-1} \\ P_4 g_4 \bar{\lambda}_2 &\le \nu_7 g_4^2 \bar{\lambda}_{max}^2 P_4^2 + \frac{1}{4}\nu_7^{-1} \end{aligned} \tag{122}$$

Similar to the way (113) was obtained, we can achieve:

$$\|P_3\|^2 \le \frac{2V_3\left(t_0\right)e^{-\bar{\imath}(t-t_0)} + 2\tilde{\mu}_3\phi_3^{-1}}{1-\overset{*}{Z}} \;\Rightarrow\; \phi_3 = \min[\phi_2, \quad \beta_3, \quad \delta_3\sigma_3] \tag{123}$$

According to (75), we can say:

$$\tilde{\mu}_3 = \frac{1}{2}\lambda_{min}P_4^2 + \frac{1}{2}\sum_{i=1}^{3}\lambda_{min}\sigma_i\theta_i^{*2} + \frac{1}{4}\sum_{i=1}^{5}\nu_i^{-1} \tag{124}$$

Thus, based on Definition (2), it is obvious from (123) that $\|P_3\|$ is uniformly exponentially bounded by use of the virtual control a_3 introduced in (39), $\|P_3\|$ will have uniform exponential stability inside to a specific ball $\mathcal{G}\left(\bar{\tau}_0\right)$, where:

$$Z(\imath) = \frac{1}{2}\sum_{i=1}^{3}\frac{\mu_i^{-1}}{\phi_3 - \imath} > 0 \;\Rightarrow\; \boxed{\imath \in [0, \phi_3)} \xrightarrow{\text{like (89)}} \qquad \mathcal{G}\left(\bar{\tau}_0\right) := \left\{ P_3 \mid \|P_3\| \le \bar{\tau}_0 = \sqrt{\frac{2\tilde{\mu}_3\phi_3^{-1}}{1-\overset{*}{Z}}} \right\} \tag{125}$$

Also, similar to the way (92) was obtained, we can achieve:

$$\|P_4\|^2 \le \frac{2V_4\left(t_0\right)e^{-\bar{\imath}(t-t_0)} + 2\tilde{\mu}_4\phi_4^{-1}}{1-\overset{*}{Z}} \;\Rightarrow\; \phi_4 = \min[\phi_3, \quad \beta_4, \quad \delta_4\sigma_4] \tag{126}$$

where:

$$\tilde{\mu}_4 = \frac{1}{2}\sum_{i=1}^{4}\lambda_{min}\sigma_i\theta_i^{*2} + \frac{1}{4}\sum_{i=1}^{7}\nu_i^{-1} \tag{127}$$

Thus, based on Definition (2), it is obvious from (126) that $\|P_4\|$ is uniformly exponentially bounded by use of the voltage-d control defined in (40). Therefore, $\|P_4\|$ will have uniform exponential stability inside to a specific ball $\mathcal{G}\left(\bar{\tau}_0\right)$, where:

$$Z(\iota) = \frac{1}{2}\sum_{i=1}^{4}\frac{\mu_i^{-1}}{\phi_4 - \iota} > 0 \Rightarrow \boxed{\iota \in [0, \phi_4)} \xrightarrow{\text{like (89)}} \qquad \mathcal{G}\left(\bar{\tau}_0\right) := \left\{ P_4 \mid \|P_4\| \leq \bar{\tau}_0 = \sqrt{\frac{2\tilde{\mu}_4\phi_4^{-1}}{1 - \overset{*}{Z}}} \right\} \tag{128}$$

Finally, the uniform exponential stability is fulfilled for the second subsystem following the Theorem (1).

4.3 | Voltage-q control stability (subsystem 3)

In the third subsystem, the control input is the voltage-q (u_q). That is, after receiving x_3, and x_2 from the two initial subsystems and considering the current control i_q^* obtained in subsystem 1 as the desired state for subsystem 3, according to (22), we can define the third subsystem as follows:

$$\boxed{\begin{aligned} \dot{x}_5 &= x_5 + F_5(x_1, x_2, x_3, x_4, x_5) + d_5 \\ \dot{x_6} &= g_6 S(u_q) + F_6(x_1, x_2, x_3, x_4, x_5, x_6) + d_6 \end{aligned}} \tag{129}$$

where $x_5 = i_q$; $x_6 = \dot{i}_q$; the states of current-q and its derivative should be tracked to i_q^* and $\dot{i}_q^*$ received from subsystem 1 as a reference; $g_6 = \frac{1}{L_q}$, $F_5 = f_5$ and $F_6 = \frac{-R_s}{L_q}x_5 - Pc_{RL}\frac{L_d}{L_q}x_3x_2 - Pc_{RL}\frac{\psi_{PM}}{L_q}x_2 + f_6$ are uncertainties; d_5 and d_6 are external disturbances; u_q is the voltage-q control in the third subsystem; and according to (35):

$$S(u_q) = \begin{cases} u_{q1}, & \text{if } u_q \geq u_{q1} \\ u_q & \text{if } u_{q2} \leq u_q \leq u_{q1} \\ u_{q2} & \text{if } u_q \leq u_{q2} \end{cases} \tag{130}$$

Likewise, we have two sub-subsystems are meant to be controlled and analyzed as in (44). In this way by defining the error of tracking as:

$$\begin{aligned} \overline{x}_5 &= x_5 - i_q^* \\ \overline{x}_6 &= x_6 - \dot{i}_q^* \end{aligned} \tag{131}$$

we alter the form of the system to the tracking form, as shown:[45]

$$\begin{aligned} P_5 &= \overline{x}_5 \\ P_6 &= \overline{x}_6 - a_5 \end{aligned} \tag{132}$$

where a_5 is the virtual control for the third subsystem. To avoid the "explosion of the complexity" derived from Wang, et al.,[28] the time derivative of the virtual control input is treated as an uncertain term in the system, according to (39). By differentiating (132), we have:

$$\begin{aligned} \dot{P}_5 &= P_6 + \overline{F}_5 + a_5 + d_5 \\ \dot{P}_6 &= g_6 S(u_q) + \overline{F}_6 - \ddot{i}_q^* + d_6 \end{aligned} \tag{133}$$

The Lyapunov functions for the virtual control and the voltage-q control, related to the third subsystem, are defined in (39) and (40) as follows:

$$\begin{aligned} V_5 &= V_4 + \frac{1}{2}\lambda_{min}\left[{P_5}^2 + \delta_5^{-1}\tilde{\theta}_5^2\right] \\ V_6 &= V_5 + \frac{1}{2}\left[P_6^2 + \delta^{-1}\lambda_{min}\tilde{\theta}_6^2\right] \end{aligned} \tag{134}$$

All proof steps are the same as the first subsystem expressed in section 4.1. In this way, we have:

$$\begin{aligned}
\lambda_{min} P_5 \overline{F}_5 &\leq \mu_5 \lambda_{min}^2 \mid P_5 \mid^2 \Lambda_5^2 + \frac{1}{4}\mu_5^{-1} r_5^2 \\
\lambda_{min} P_5 d_5 &\leq \nu_8 \lambda_{min}^2 \mid P_5 \mid^2 d_{max(5)}^2 + \frac{1}{4}\nu_8^{-1} \\
P_6 \overline{F}_6 &\leq \mu_6 \Lambda_6^2 P_6^2 + \frac{1}{4}\mu_6^{-1} r_6^2 \\
P_6 d_6 &\leq \nu_9 d_{max(6)}^2 P_6^2 + \frac{1}{4}\nu_9^{-1} \\
-P_6 \ddot{\imath}_q^* &\leq \nu_{10} \Omega^2 P_6^2 + \frac{1}{4}\nu_{10}^{-1} \\
P_6 g_6 \bar{\lambda}_3 &\leq \nu_{11} g_6^2 \bar{\lambda}_{max}^2 P_6^2 + \frac{1}{4}\nu_{11}^{-1}
\end{aligned} \tag{135}$$

where $\mid \ddot{\imath}_q^* \mid \leq \Omega$. Similar to how (113) was obtained, we can achieve:

$$\| P_5 \|^2 \leq \frac{2V_5\left(t_0\right) e^{-\bar{\imath}(t-t_0)} + 2\tilde{\mu}_5 \phi_5^{-1}}{1 - \overset{*}{Z}} \Rightarrow \phi_5 = \min[\phi_4, \quad \beta_5, \quad \delta_5 \sigma_5] \tag{136}$$

where:

$$\tilde{\mu}_5 = \frac{1}{2}\lambda_{min} P_6^2 + \frac{1}{2}\sum_{i=1}^{5} \lambda_{min} \sigma_i \theta_i^{*2} + \frac{1}{4}\sum_{i=1}^{8} \nu_i^{-1} \tag{137}$$

Thus, based on Definition (2), it is obvious from (139) that $\| P_5 \|$ is uniformly exponentially bounded by use of the virtual control a_5. Therefore, $\| P_5 \|$ will have uniform exponential stability inside to a specific ball $\mathcal{G}\left(\bar{\tau}_0\right)$, where:

$$Z(\imath) = \frac{1}{2}\sum_{i=1}^{5} \frac{\mu_i^{-1}}{\phi_5 - \imath} > 0 \Rightarrow \boxed{\imath \in [0, \phi_5)} \xrightarrow{\text{like (89)}} \qquad \mathcal{G}\left(\bar{\tau}_0\right) := \left\{ P_5 \mid \| P_5 \| \leq \bar{\tau}_0 = \sqrt{\frac{2\tilde{\mu}_5 \phi_5^{-1}}{1 - \overset{*}{Z}}} \right\} \tag{138}$$

Similar to how (92) was obtained, we can achieve:

$$\| P_6 \|^2 \leq \frac{2V_6\left(t_0\right) e^{-\bar{\imath}(t-t_0)} + 2\tilde{\mu}_6 \phi_6^{-1}}{1 - \overset{*}{Z}} \Rightarrow \phi_6 = \min[\phi_5, \quad \beta_6, \quad \delta_6 \sigma_6] \tag{139}$$

where:

$$\tilde{\mu}_6 = \frac{1}{2}\sum_{i=1}^{6} \lambda_{min} \sigma_i \theta_i^{*2} + \frac{1}{4}\sum_{i=1}^{11} \nu_i^{-1} \tag{140}$$

Thus, based on Definition (2), it is obvious from (140) that $\| P_6 \|$ is uniformly exponentially bounded. Therefore, $\| P_6 \|$ will have uniform exponential stability inside to a specific ball $\mathcal{G}\left(\bar{\tau}_0\right)$, where:

$$Z(\imath) = \frac{1}{2}\sum_{i=1}^{6} \frac{\mu_i^{-1}}{\phi_6 - \imath} > 0 \Rightarrow \boxed{\imath \in [0, \phi_6)} \xrightarrow{\text{like (89)}} \qquad \mathcal{G}\left(\bar{\tau}_0\right) := \left\{ P_6 \mid \| P_6 \| \leq \bar{\tau}_0 = \sqrt{\frac{2\tilde{\mu}_6 \phi_6^{-1}}{1 - \overset{*}{Z}}} \right\} \tag{141}$$

Finally, the uniform exponential bound is fulfilled for the third subsystem of the EMLA following Theorem (1).
In the following section, an investigation into the performance of the RDSC will be conducted. This investigation will encompass two distinct cycle duties, each of which will involve various load tasks for the EMLA.

5 | NUMERICAL VALIDITY

To validate the effectiveness of the RDSC, we conducted a comprehensive performance analysis using three subsystems as described in equations (30), to simulate the behavior of the EMLA, modeled in section 2. The analysis was carried out through two duties with different loads, where the EMLA tracked the same reference trajectories. During this analysis, uncertainties, which are assumed unknown, were considered in the first subsystem, according to the EMLA specifications provided in Table

1 and (24), as follows:

$$\begin{aligned} F_1 = f_1, F_2 = -I_{eq}^{-1}(b_{eq}x_2 + k_{eq}x_1) + f_2 \\ \Rightarrow\ f_1 = 0,\ f_2 = 2\,(5 + 0.1\cos(0.5\pi t))\ \text{Arctan}(900t) \end{aligned} \tag{142}$$

in the second subsystem:

$$\begin{aligned} F_3 = f_3,\ F_4 = \frac{-R_s}{L_d}x_3 + Pc_{RL}\frac{L_q}{L_d}i_q^* x_2 + f_4 \\ \Rightarrow\ f_3 = 0,\ f_4 = -0.1\sin(0.5\pi t) \end{aligned} \tag{143}$$

and in the third subsystem:

$$\begin{aligned} F_5 = f_5,\ F_6 = \frac{-R_s}{L_q}x_5 - Pc_{RL}\frac{L_d}{L_q}x_3x_2 - Pc_{RL}\frac{\psi_{PM}}{L_q}x_2 + f_6 \\ \Rightarrow\ f_5 = 0,\ f_6 = 0.3\cos(0.5\pi t) \end{aligned} \tag{144}$$

In addition, we considered the external disturbances affected by integrating loads into all three subsystems, as follows:

$$\begin{aligned} d_1 = d_3 = d_5 = 0 \\ d_2 = f_{eq}F_L \\ d_4 = 2\,\sin\left(3\pi t + \frac{\pi}{7}\right) \\ d_6 = \text{rand}(2) - 0.3 \end{aligned} \tag{145}$$

The load force, denoted by F_L, refers to the force required by the actuator to move the load in the desired direction, taking into account the load's weight and friction. The weight and distribution of the load are critical factors in determining the load force required, where a heavier load with an uneven distribution will require a higher load force compared to a lighter, more evenly distributed load. To evaluate the effectiveness of our RDSC design for EMLAs, we conducted two different duties involving loading and unloading procedures with various nonlinear load forces, which are supposed to be unknown. These duties included forward and backward motions to represent different movements, which tested the RDSC's capability to control the EMLA. Our analysis focused on assessing the performance of the RDSC under different load conditions, motion types, and undesired forces, the results of which will provide valuable insights into the EMLA's effectiveness for practical applications.

Figure 4 illustrates the goal trajectories of the EMLA modeled during both duty phases. The actuator is designed to move linearly forward from its initial position, as indicated by the blue line, until it reaches a point 100 cm away from the starting point in the first step. In the second step, the actuator returns halfway to its previous position, stopping at a point 50 cm from the starting point, as shown by the green line. The actuator then moves forward again in the third step, following the red line, until it reaches a point 100 cm away from the starting point. In the final and fourth step, the actuator returns to its original starting position, following the orange line.

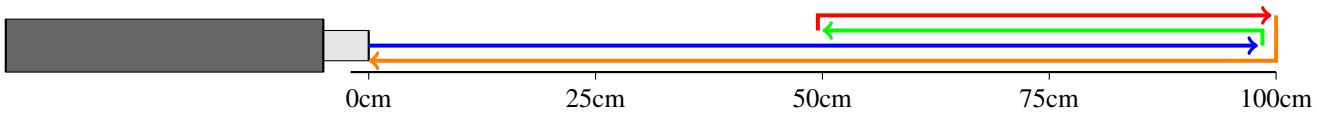

FIGURE 4 EMLA trajectories for both duty cycles (blue line: step 1, green line: step 2, red line: step 3, orange line: step 4).

Using the EMLA's specification provided in Table 1, the control performance is also investigated. Further, Table 2 presents information on the parameters used in the control design and saturation levels applied to both the current and voltage control inputs, which were kept constant across both duties. As per equation (47) and Table 1, the upper and lower limits for the motor current, i_{q1}^* and i_{q2}^*, respectively, are set to 7.9 A and -7.9 A. In addition, based on (117) and (130), and in accordance with the motor's specifications, the acceptable maximum and minimum voltage limits are set to 380 V for u_{q1} and u_{d1}, and -380 V for u_{q2} and u_{d2}. It should be emphasized that the design control parameters for the RDSC of the EMLA are limited to only four, namely, β, ζ, δ, and σ. These few parameters contribute to the simplicity of the control process for the entire EMLA system, and the equations are essential to design of the RSDC situated within boxes for convenient reference, including (30), (36), (39), (40), and (41). During duty cycles 1 and 2, we introduced a variety of loads to evaluate the performance of the RDSC in the presence of heavy and nonlinear loads, as well as to assess its robustness against unknown forces acting as uncertainties and disturbances, as defined in (142) to (145).

TABLE 2 Control parameters

Gain	Value
$\beta_1, \beta_2, \beta_3, \beta_4, \beta_5, \beta_6$	60
$\zeta_1, \zeta_2, \zeta_3, \zeta_4, \zeta_5, \zeta_6$	0.01
$\delta_1, \delta_2, \delta_3, \delta_4, \delta_5, \delta_6$	100
$\sigma_1, \sigma_2, \sigma_3, \sigma_4, \sigma_5, \sigma_6$	0.01
i^*_{q1}	7.9
i^*_{q2}	-7.9
$u_{d1},\ u_{q1}$	380
$u_{d2},\ u_{q2}$	-380

5.1 | Duty cycle 1

In this duty, we considered two distinct load types (load 11 and load 12), as illustrated in Figure 5 and 6(a) and the equations in (145) and (146):

$$\begin{aligned} &\textbf{Load 11:}\quad F_L = 1000\ [0.1sin(5t) + 80] \\ &\textbf{Load 12:}\quad F_L = 500\ [0.1sin(5t) + 80] \end{aligned} \tag{146}$$

In this duty, we considered significantly heavy and constant loads (80kN and 40kN), accompanied by a nonlinear component represented by a sine function to enable a hard distribution of the load. Notably, the amplitude of Load 11 is twice that of Load 12. Based on the information provided by Figure 5, 6a, and 8, it can be observed that the loading and unloading times for duty 1, as well as the time spent tracking the trajectory, are as follows: at 145 s into the duty, Load 11 is applied to the EMLA at a position of 100 cm. The load is then unloaded at 320 s, when the EMLA has moved to a position of 50 cm (green line step). After this, at 420 s, Load 12 is picked up by the EMLA at a position of 100 cm. The load is then transported to its origin, arriving at 600 s, where it is subsequently unloaded (orange line step).

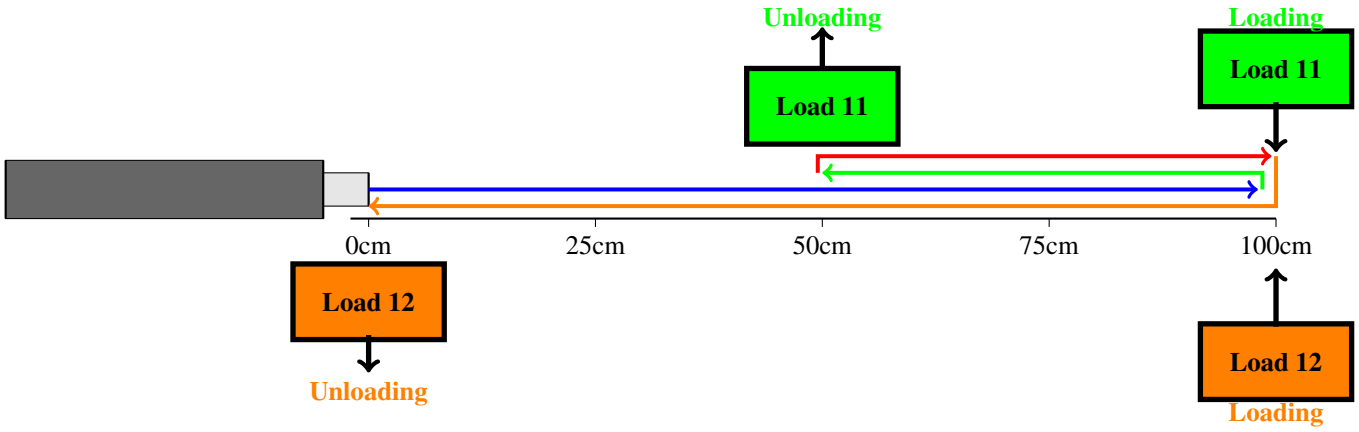

FIGURE 5 EMLA duty 1.

5.2 | Duty cycle 2

In this duty, we introduced a wider range of loads, while keeping the same tracking process, control parameters, and unknown uncertainties as in the previous duty. As illustrated in (147) and Figure 6b, it is apparent that the amplitude of the constant component and frequency of the sine function of the loads are lower than the previous duty, while the number of loading and unloading operations is higher. In addition, the constant load component for the present duty is comparatively lighter than that of the previous duty, with magnitudes of 72 kN, 24 kN, and 36 kN as the dominant parts:

$$
\begin{aligned}
&\textbf{Load 21:}\ F_L = 1000\ [0.1sin(3t) + 72] \\
&\textbf{Load 22:}\ F_L = 333.33\ [0.1sin(3t) + 72] \\
&\textbf{Load 23:}\ F_L = 500\ [0.1sin(3t) + 72] \\
&\textbf{Load 24:}\ F_L = 1000\ [0.1sin(3t) + 72]
\end{aligned} \tag{147}
$$

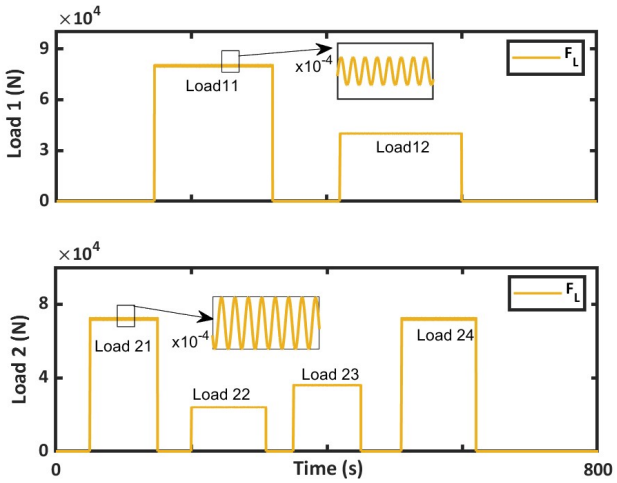

FIGURE 6 Loads: Load 1: Duty 1, Load 2: Duty 2.

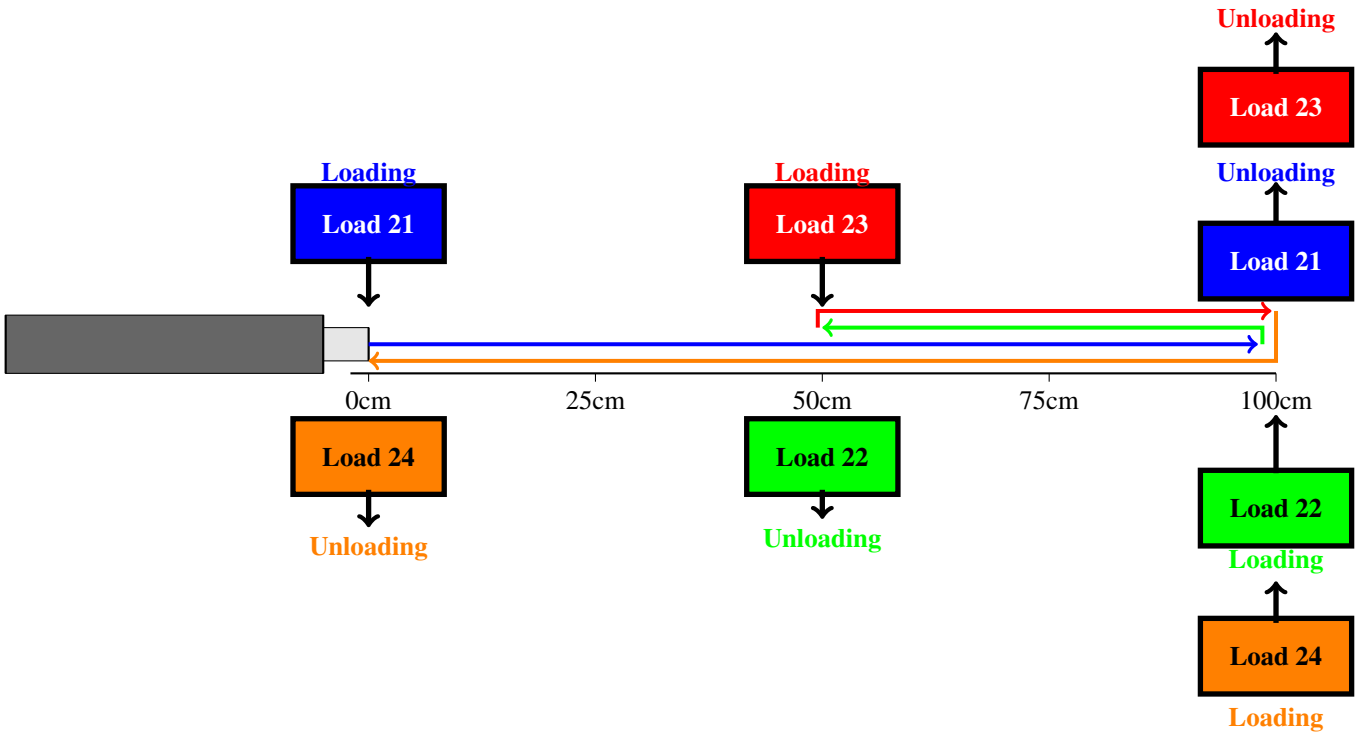

FIGURE 7 EMLA duty 2.

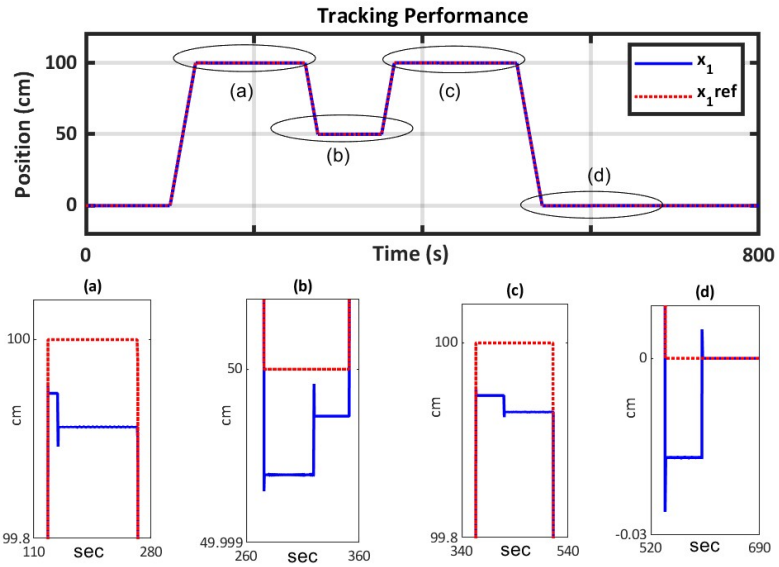

FIGURE 8 Duty 1: Position tracking performance: (a) loading 11, (b) unloading 11, (c) loading 12, (d) unloading 12.

The loading and unloading positions can be observed in Figure 6(b) and 7. In contrast to duty 1, where the EMLA only carried loads during its backward movement, this duty includes additional loading tasks for transporting Load 21 and Load 23 forwardly. Moreover, the EMLA carries Load 22 and Load 24 during its return movement. It is noteworthy that Load 21 and Load 24 are the heaviest among those considered in this duty, while Load 22 has a third of their amplitude and Load 23 has half of their amplitude. Therefore, in this duty and according to Figure 6(b) and, 7, the EMLA is responsible for carrying four loads, namely Load 21, Load 22, Load 23, and Load 24. The EMLA carries Load 21 from the origin position, 50 s after starting the duty. It then disposes of Load 21 at a position 100 cm away from the starting point, at 150 s into the duty. After unloading Load 21, the EMLA carries Load 22 to the same position and disposes of it at a distance of 50 cm from the origin, at 310 s into the duty. Subsequently, at 350 s into the duty, the EMLA carries Load 23 to the same position and disposes of it 100 cm away from the initial point using a forward motion approach, at 450 s into the duty. Finally, the EMLA carries Load 24 at 510 s into the duty and disposes of it at the original point using a feedback motion approach. It is noteworthy that the duration of rest during duty 2 is slightly longer than that during duty 1 at the 50-cm position, due to the increased loading and unloading responsibilities. Similarly, the final step of loading and unloading in duty 2 takes longer than in duty 1, also due to the increased responsibilities. Therefore, it can be observed that for duty 2, the maximum load considered is 10 percent lighter that for duty 1, even though the number of loading and unloading duties doubled. Furthermore, the loading and unloading process is faster than in the previous duty, as depicted in Figure 6. All these variations have been examined to assess the performance of RDSC for the EMLA under different conditions.

5.3 | RDSC results for both duties

Figure 8 illustrates the performance of the RDSC in tracking the reference position of the EMLA in duty 1. It is evident from the results that the tracking performance is exceptional, even in the presence of load effects and uncertainties. Specifically, the true position state x_1 exhibits accurate and fast tracking of the reference value $x_{1\text{ref}}$, and the figure indicates that the tracking error accuracy is approximately $4x10^{-2}$ cm when the EMLA is unloaded, while the error increases to $8x10^{-2}$ cm when the EMLA is loaded. Notably, when the EMLA is not loaded and there is a consistency in position, as shown in part (d) after 600 s of Figure 8, the tracking error is $2x10^{-8}$, even in the presence of unknown uncertainties. Thus, the error of $4x10^{-2}$ occurs only at the moment of stopping in a new position. Similar to duty 1, Figure 9 demonstrates the tracking performance of the RDSC for EMLA in duty 2. It is evident from the results that the tracking performance is also exceptional in duty 2, even in the presence of more variable load effects and the same uncertainties. The figure indicates that the tracking error accuracy is approximately $4x10^{-2}$ cm when the EMLA is not loaded, while the error increases to $6x10^{-2}$ cm when the EMLA is loaded.

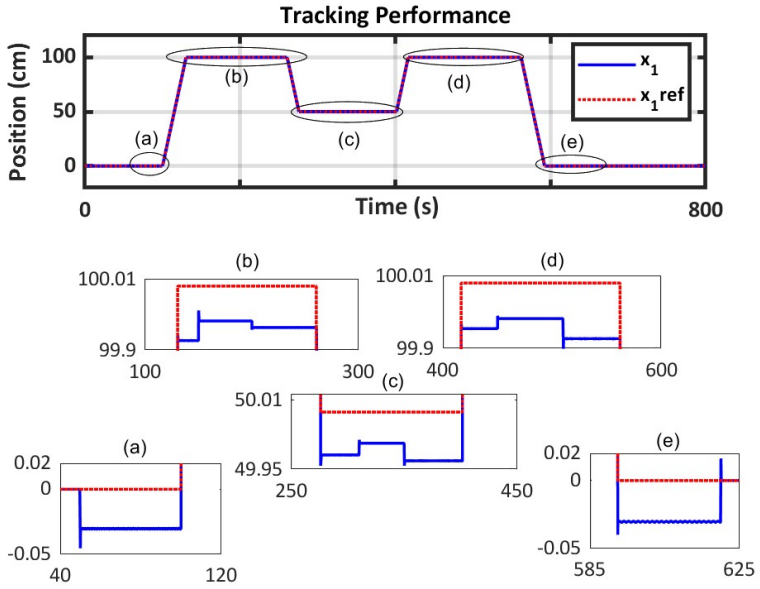

FIGURE 9 Duty 2: Position tracking performance: (a) loading 21, (b) unloading 21 and loading 22, (c) unloading 22 and loading 23, (d) unloading 23 and loading 24, (e) unloading 24.

Notably, when the EMLA is not loaded and there is no change in position, as shown in parts (a), before 45 s and (d) after 625 s of Figure 9, the tracking error is similarly $2x10^{-8}$, even in the presence of uncertainties. Likewise, the error of $4x10^{-2}$ occurs only during the stopping moment. As shown in Figures 8 and 9, the accuracy of position tracking using the RDSC with loads is better in duty 2 than in duty 1. This result is sensible because, in duty 2, although the number of loads is greater, the magnitudes of the loads are lower than those in duty 1.

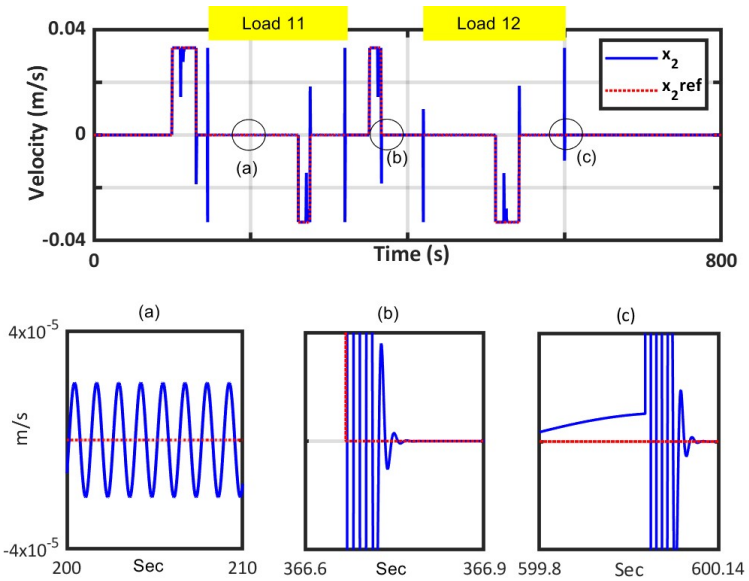

FIGURE 10 Duty 1: Velocity tracking performance.

Figure 10 displays the performance of linear velocity tracking using the RDSC in duty 1. The figure illustrates that there are

pulses in the real velocity when the load status changes. The duration for which the loads are carried by the EMLA in duty 1 has been delineated by yellow boxes in Figure 10. The figure illustrates that most of the pulses correspond to the changing status of load tasks. The error in the reference velocity tracking is approximately $3x10^{-5}$ m/s, and the tracking speed in this duty is about 0.1 s. Similar to duty 1, Figure 11 demonstrates the performance of linear velocity tracking using the RDSC in duty 2. The figure also shows that the pulses remain in real velocity when the load status changes. The duration for which the loads are carried by the EMLA in duty 2 has been delineated by yellow boxes in Figure 11. The figure illustrates that most of the pulses correspond to the changing status of load tasks, as in the previous duty. The error in reference velocity tracking is approximately $2.5x10^{-5}$ m/s, and the tracking speed in this duty is about 0.07 s.

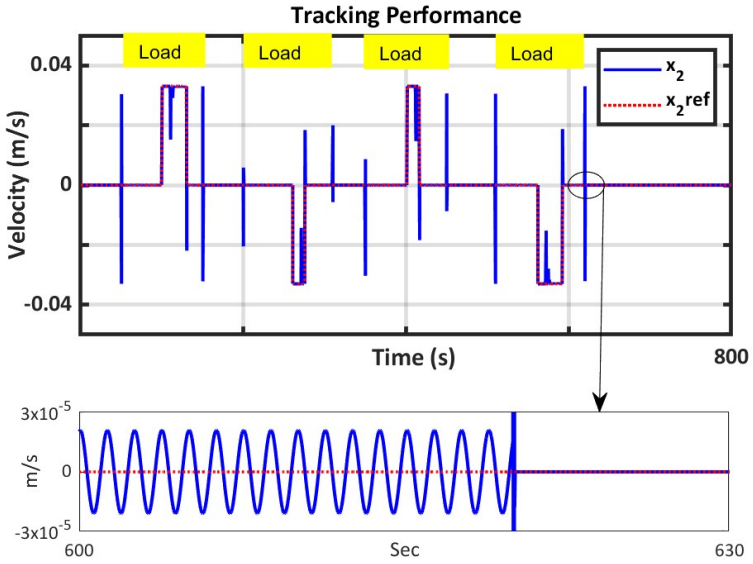

FIGURE 11 Duty 2: Velocity tracking performance.

It is worth noting that the number of velocity pulses in duty 2 is greater than that in duty 1, and this can be attributed to the higher number of loading tasks in duty 2. In Figure 12, which pertains to duty 1, the real and saturated values of i_q and u_q are shown with blue and red lines, respectively, confirming the capability of the RDSC under input constraints. Furthermore, according to the second subsystem, i_d is expected to track zero, which is achieved with an accuracy of 0.03 A. The highest pulse in i_d is observed during the loading of Load 11 at 145 s. In addition, the value of u_d is maintained below 30 V to force i_d to track zero. Similar to duty 1, Figure 13, pertaining to duty 2, depicts the actual and saturated values for i_q and u_q respectively, represented by blue and red lines. This serves as a confirmation of the RDSC's capability under input constraints. Moreover, as per the second subsystem's requirement, i_d is expected to track zero, which is achieved with an accuracy of 0.025 A. The highest pulse in i_d is attributed to Load 24 at the time of loading, which occurs at 510 s. In addition, the value of u_d is maintained below 20 V to force i_d to track zero. Due to the higher frequency of load changes in duty 2, there are more variations and spikes in currents and voltages. Figure 14 presents a comparison of the produced torques in both duties. According to (6), because the model-based EMLA's produced torque is dependent on the i_q value and because i_q is constrained to a range of -7.9 A to 7.9 A, the maximum torque value for both duties is consistent and identical, i.e., 12.7 N.m. However, due to the longer duration required by the EMLA to carry the loads in duty 1, the torque associated with this duty remains the maximum value, greater than duty 2. Furthermore, the starting and finishing times of the produced torque in duty 2 are earlier and later, respectively, compared to duty 1 because of the more extended loading and unloading tasks. The length of the boxes situated in Figure 14 represents the duration for which the EMLA carries the loads, facilitating an easy comprehension of the torque patterns produced. Specifically, the yellow boxes correspond to duty 1, whereas the red boxes pertain to duty 2. To summarize, Tables 3 and 4 provide an overview of the accuracy and speed control performance of the RSDC system in controlling the modeled EMLA to follow the desired trajectories in both duties.

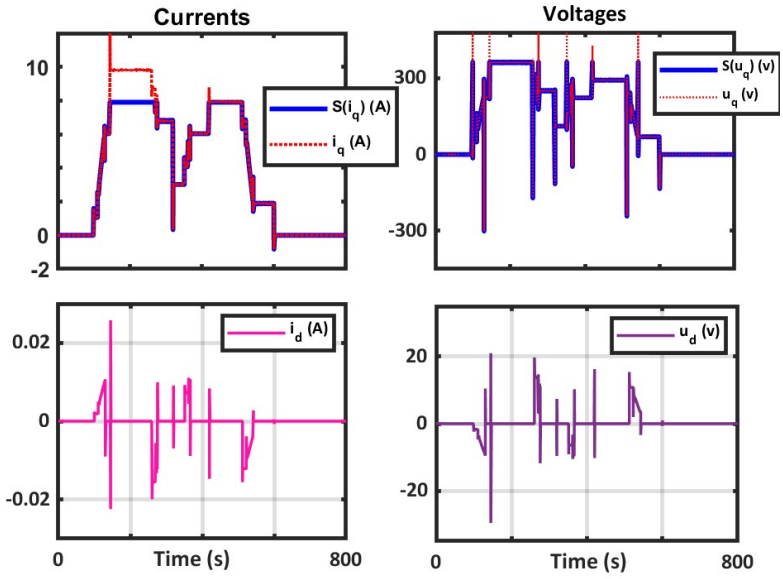

FIGURE 12 Duty 1: Currents and voltages.

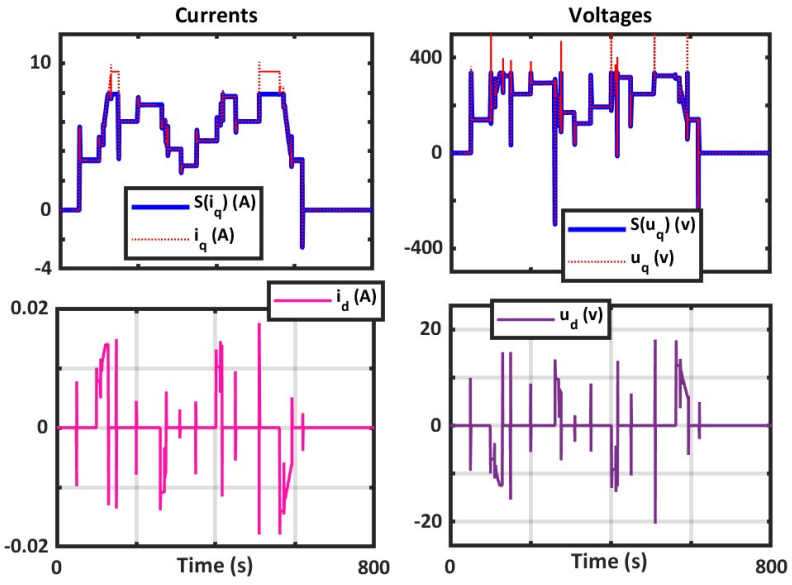

FIGURE 13 Duty 2: Currents and voltages.

As previously mentioned, the control position accuracy in duty 2 is superior to that in duty 1 due to the lighter loads involved. Furthermore, the speed of position convergence in both duties is relatively similar and fast. This also holds true for the error convergence when tracking reference velocity using the RDSC, although the control velocity in duty 2 exhibits a slightly better performance when compared to the first duty. In essence, these findings indicate that the RSDC system effectively controls the EMLA in both duties with good accuracy and speed control performance.

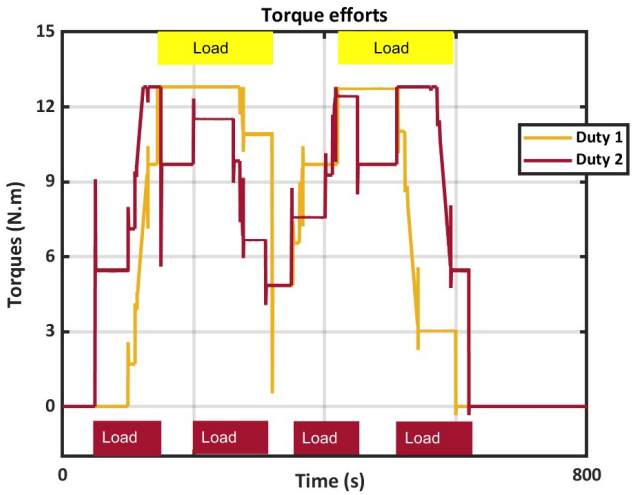

FIGURE 14 Duty 1,2: Torques.

TABLE 3 Position tracking x_1

Convergence quality		
Scenarios	**Error (cm)**	**Speed (sec)**
Duty 1	$8x10^{-2}$	0.07 sec
Duty 2	$6x10^{-2}$	0.07 sec

TABLE 4 Velocity tracking x_2

Convergence quality		
Scenarios	**Error (m/s)**	**Speed (sec)**
Duty 1	$3x10^{-5}$	0.1 sec
Duty 2	$2.5x10^{-5}$	0.07 sec

6 | CONCLUSION

The research findings demonstrated the studied EMLA system's capability to generate all necessary state variables, including torques acting on the motor and load side, to achieve the prescribed dynamics. It also included a thorough analysis and control of the EMLA, demonstrating how it can be structured and understood through the use of a robust adaptive backstepping control in a six-order NSFF, which has rarely been utilized before for EMLAs facing input constraints, external disturbance, and uncertainties. In other words, we presented and developed a robust control approach called the RDSC for a complex EMLA system with multi-stage gearing driven by a PMSM in three subsystems, which was capable of tracking reference linear trajectories with uniformly exponential stability, without requiring knowledge of uncertain parameters and functional load conditions. In addition, to enable analytic computations and prevent the "complexity explosion" associated with the backstepping concept, the RDSC treated the time derivative of the virtual control input as an uncertainty term. Our findings demonstrated the potential of the RDSC for the EMLA in NSFFs and provided a straightforward form control for future research in this area. One potential avenue for future research is to explore the extension of the proposed RDSC approach to other types of actuators, such as pneumatic cylinders or hydraulic systems. By expanding the applicability of the RDSC approach to various fields and industries, new avenues for its implementation can be opened up. Another interesting direction for future research is the integration of the RDSC approach into machine learning techniques to enhance the performance of EMLAs in NSFFs. By integrating machine learning using the RDSC approach, it may be possible to achieve an even better control performance and extend the applicability of this approach to various dynamic systems.

7 | ACKNOWLEDGMENT

We declare that there are no conflicts of interest to disclose. We also acknowledge the support and funding provided by the Business Finland partnership project "Future all-electric rough terrain autonomous mobile manipulators" (Grant No. 2334/31/2022). And, we confirm that this work is original and has not been published elsewhere, nor is it currently under consideration for publication elsewhere.

References

1. Bischoff R, Guhl T. The strategic research agenda for robotics in europe [industrial activities]. *IEEE Robotics & Automation Magazine* 2010; 17 (1): 15–16.

2. Daily M, Medasani S, Behringer R, Trivedi M. Self-driving cars. *Computer*; 50 .

3. Badue C, Guidolini R, Carneiro RV, et al. Self-driving cars: A survey. *Expert Systems with Applications* 2021; 165 : 113816.

4. Habibnejad Korayem M, Ghobadi N, Fathollahi Dehkordi S. Designing an optimal control strategy for a mobile manipulator and its application by considering the effect of uncertainties and wheel slipping. *Optimal Control Applications and Methods* 2021; 42 (5): 1487–1511.

5. Cao W, Mecrow BC, Atkinson GJ, Bennett JW, Atkinson DJ. Overview of electric motor technologies used for more electric aircraft (MEA). *IEEE Transactions on Industrial Electronics* 2011; 59 (9): 3523–3531.

6. Li J, Yu Z, Huang Y, Li Z. A review of electromechanical actuation system for more electric aircraft. In: *2016 IEEE International Conference on Aircraft Utility Systems (AUS)*. ; 2016: 490–497.

7. Fleming KL, Brown AL, Fulton L, Miller M. Electrification of medium-and heavy-Duty ground transportation: Status report. *Current Sustainable/Renewable Energy Reports* 2021; 8 (3): 180–188.

8. Nagel N. Actuation challenges in the more electric aircraft: Overcoming hurdles in the electrification of actuation systems. *IEEE Electrification Magazine* 2017; 5 (4): 38–45.

9. Lequesne B. Automotive electrification: The nonhybrid story. *IEEE Transactions on Transportation Electrification* 2015; 1 (1): 40–53.

10. Boldea I, Nasar SA. Linear electric actuators and generators. *IEEE Transactions on Energy Conversion* 1999; 14 (3): 712–717.

11. Knabe C, Lee B, Orekhov V, Hong D. Design of a compact, lightweight, electromechanical linear series elastic actuator. In: . v: 46377 . *American Society of Mechanical Engineers*. ; 2014: p: V05BT08A014.

12. Redekar A, Deb D, Ozana S. Functionality Analysis of Electric Actuators in Renewable Energy Systems—A Review. *Sensors* 2022; 22 (11): 4273.

13. Hassan W, Wang B. Efficiency optimization of PMSM based drive system. In: *IEEE 7th International Power Electronics and Motion Control Conference*. ; 2012: 1027–1033.

14. Achour HB, Ziani S, Chaou Y, El Hassouani Y, Daoudia A. Permanent magnet synchronous motor PMSM control by combining vector and PI controller. *WSEAS Transactions on Systems and Control* 2022; 17 : 244–249.

15. Li LB, Sun HX, Chu JD, Wang GL. The predictive control of PMSM based on state space. In: . 2 . *Proceedings of the 2003 International Conference on Machine Learning and Cybernetics (IEEE Cat. No. 03EX693)*. ; 2003: 859–862.

16. Hagras AA. Nonlinear adaptive extended state space predictive control of permanent magnet synchronous motor. *International Transactions on Electrical Energy Systems* 2019; 29 (1): e2677.

17. Caracciolo R, Richiedei D. Optimal design of ball-screw-driven servomechanisms through an integrated mechatronic approach. *Mechatronics* 2014; 24 (7): 819–832.

18. Zhang X. *Strict-Feedback Nonlinear Systems: Gain Control Design*. v: 7 . Springer Nature . 2023.

19. Sun X, Yu H, Yu J, Liu X. Design and implementation of a novel adaptive backstepping control scheme for a PMSM with unknown load torque. *IET Electric Power Applications* 2019; 13 (4): 445–455.

20. Tan LN, Pham TC. Optimal tracking control for PMSM with partially unknown dynamics, saturation voltages, torque, and voltage disturbances. *IEEE Transactions on Industrial Electronics* 2021; 69 (4): 3481–3491.

21. Yin Z, Wang B, Du C, Zhang Y. Barrier-Lyapunov-function-based backstepping control for PMSM servo system with full state constraints. In: *22nd International Conference on Electrical Machines and Systems (ICEMS)*. ; 2019: 1–5.

22. Astolfi A, Karagiannis D, Ortega R. *Nonlinear and Adaptive Control with Applications.*. v: 187 . Springer . 2008.

23. Sadati S, Parvar MS, Menhaj MB, Bahrami M. Backstepping controller design using neural networks for a fighter aircraft. *European Journal of Control* 2007; 13 (5): 516–526.

24. Wang X, Chen Y, Lu Y, Li X, He W. Dynamic surface method–based adaptive backstepping control for the permanent magnet synchronous motor on parameter identification. *Proceedings of the Institution of Mechanical Engineers, Part I: Journal of Systems and Control Engineering* 2019; 233 (9): 1172–1181.

25. Luo R, Deng Y, Xie Y. Neural network backstepping controller design for uncertain permanent magnet synchronous motor drive chaotic systems via command filter. *Frontiers in Physics* 2020; 8 : 182.

26. Zheng X, Xue L, Wang P, Li J, Shen Z. Parameters adaptive backstepping control of PMSM using DTC method. In: . 236 . *E3S Web of Conferences; EDP Sciences*. ; 2021: 04028.

27. Li T, Liu X, Yu H. Backstepping non-singular terminal sliding mode control for PMSM with finite-time disturbance observer. *IEEE Access* 2021; 9 : 135496–135507.

28. Wang F, Hua C, Zong Q. Attitude control of reusable launch vehicle in re-entry phase with input constraint via robust adaptive backstepping control. *International Journal of Adaptive Control and Signal Processing* 2015; 29 (10): 1308–1327.

29. Lu S, Wang X. Command filtering-based neural network control for fractional-order PMSM with input saturation. *IEEE Access* 2019; 7 : 137811–137822.

30. Lu S, Wang X. Observer-based command filtered adaptive neural network tracking control for fractional-order chaotic PMSM. *IEEE Access* 2019; 7 : 88777–88788.

31. Liu XD, Li K, Zhang CH. Improved backstepping control with nonlinear disturbance observer for the speed control of permanent magnet synchronous motor. *Journal of Electrical Engineering & Technology* 2019; 14 : 275–285.

32. Ali N, Alam W, Pervaiz M, Iqbal J. Nonlinear adaptive backstepping control of permanent magnet synchronous motor. *Revue Roumaine des Sciences Techniques–Serie Electrotechnique et Energetique* 2021; 66 (1): 15–20.

33. Tan LN, Cong TP, Cong DP. Neural network observers and sensorless robust optimal control for partially unknown PMSM with disturbances and saturating voltages. *IEEE Transactions on Power Electronics* 2021; 36 (10): 12045–12056.

34. Coban R. Adaptive backstepping sliding mode control with tuning functions for nonlinear uncertain systems. *International Journal of Systems Science* 2019; 50 (8): 1517–1529.

35. Lin FJ, Lee CC. Adaptive backstepping control for linear induction motor drive to track periodic references. *IEEE Proceedings-Electric Power Applications* 2000; 147 (6): 449–458.

36. Pillay P, Krishnan R. Modeling of permanent magnet motor drives. *IEEE Transactions on Industrial Electronics* 1988; 35 (4): 537–541.

37. Cahill D, Adkins B. The permanent-magnet synchronous motor. *Proceedings of the IEEE - Part A: Power Engineering* 1962; 109 : 483–491.

38. Alacoque JC. Surface-mounted permanent-magenet synchronous motor. *Direct Eigen Control for Induction Machines and Synchronous Motors* 2013; 1st Edition : 65–119.

39. Yousfi BE, Soualhi A, Medjaher K, Guillet F. Electromechanical modeling of a motor–gearbox system for local gear tooth faults detection. *Mechanical Systems and Signal Processing* 2022; 166 .

40. Qiao G, Liu G, Shi Z, Wang Y, Ma S, Lim TC. A review of electromechanical actuators for more/all electric aircraft systems. *Proceedings of the Institution of Mechanical Engineers, Part C: Journal of Mechanical Engineering Science* 2018; 232 (22): 4128–4151.

41. Hollander KW. Design of lightweight lead screw actuators for wearable robotic applications. *ASME Journal of Mechanical Design* 2006; 128 : 644–648.

42. Karam W, Mare JC. Modelling and simulation of mechanical transmission in roller-screw electromechanical actuators. *Aircraft Engineering and Aerospace Technology* 2009.

43. Lu T, Lan W. Composite nonlinear feedback control for strict-feedback nonlinear systems with input saturation. *International Journal of Control* 2019; 92 (9): 2170–2177.

44. Chai S, Wang L, Rogers E. Model predictive control of a permanent magnet synchronous motor with experimental validation. *Control Engineering Practice* 2013; 21 (11): 1584–1593.

45. Tong S, Li Y. Fuzzy adaptive robust backstepping stabilization for SISO nonlinear systems with unknown virtual control direction. *Information Sciences* 2010; 180 (23): 4619–4640.